ARTICLE

https://doi.org/10.1590/2317-4889202320220079

BJGEO Brazilian Journal of Geology

Zircon U-Pb dating and petrogenesis of the São José do Campestre Granite Complex, NE Brazil: an example of neoarchean mantle-derived post-collisional magmatism

Zorano Sérgio de Souza[1]*, Elton Luiz Dantas[2], Elson Paiva Oliveira[3], Frederico Castro Jobim Vilalva[1], Rafael Gonçalves da Motta[4], Hervé Martin[5#], Samir do Nascimento Valcácio[6]

Abstract

This article discusses the geochemical and petrological evolution of the São José do Campestre granite complex (SJCgr), the last Neoarchean plutonic event so far described in the São José do Campestre massif in NE Brazil. We report field, petrographic, zircon U-Pb dating, and whole rock and mineral chemistry for representative SJCgr samples. Laser ablation zircon U-Pb data indicate that the granite emplacement took place at 2664 ± 13 Ma. The rocks comprising the SJCgr have relatively well-preserved primary textures and fabrics and compositions varying from gabbro to syenogranite. Major and trace element contents reveal a metaluminous, calc-alkaline through transitional to alkaline signature, and LILE- and LREE-enriched series analogous to late Archean sanukitoid and modern arc granitoid. The evolution of the SJCgr is envisaged as follows: (1st) partial melting of a metasomatized mantle (2.5–3.0 GPa, ~85–102 km, 1,000–1,200°C), generating a basaltic to basaltic andesitic magma; (2nd) fractional crystallization (FC) of olivine at mantle or lower crustal depth, leading to the parental magmas of the magmatic series; and (3rd) 40–15% FC of olivine gabbro-norite and olivine monzonite cumulates (400–600 MPa, 15–23 km). The SJCgr shares similarities with post-collisional granitoids and, thus, would represent the last Neoarchean episode of mantle-derived magma in Northeastern Brazil.

KEYWORDS: sanukitoid; geochronology; geochemistry; petrogenesis; tectonics.

INTRODUCTION

The Archean Eon has long been considered the most important period of continental growth and is characterized by much higher geothermal gradients than today (Richter 1988, Abbott *et al.* 1994, Vanderhaeghe *et al.* 2019). These features resulted in the genesis of komatiites and an enormous volume of tonalite-trondhjemite-tonalite-granodiorite (TTG) magmatism (Barker and Arth 1976, Condie 1981, Martin 1986, 1994, Herzberg 2016, Laurent *et al.* 2014, 2020). Potassium-rich alkaline granites (Achaean crustal progeny granites; *cf.* Nebel *et al.* 2018) appear in the late Archean, and their generation has been associated with partial melting of older crustal sources, mainly TTG (Jahn *et al.* 1981, Martin 1986, Sylvester 1994, Laurent *et al.* 2014). On the contrary, studies in well-investigated areas suggest that these granites are mantle-derived, formed through variable degrees of interaction between mantle peridotite and TTG melts. In this case, they are generally referred to as sanukitoid or Closepet-type plutons (Stern and Hanson 1991, Jayananda *et al.* 1995, 2000, 2018, Smithies and Champion 2000, Moyen *et al.* 2001, 2003, Martin *et al.* 2005, 2009, Moyen *et al.* 2001, 2003, Laurent *et al.* 2014, Guo *et al.* 2018, Nebel *et al.* 2018).

Recent analogs of Archean TTG, the so-called adakites, are formed in modern subduction zones and are distinguished by higher Mg, Ni, and Cr than Archean TGG (Martin 1999, Smithies 2000, Martin *et al.* 2005, Castillo 2006). Their generation involves a complex interaction system, in which the adakitic magma, once formed by partial melting of subducted oceanic crust, interacts with the overlying mantle and/or the lower arc crust (Defant and Drummond 1990, Drummond and Defant 1990, Sen and Dunn 1994, Maury *et al.* 1996, Stern and Kilian 1996, Rapp *et al.* 1999, Castillo 2012).

The gradual cooling of the Earth led to the progressive generation of the continental crust, of which two-thirds to three-quarters may have formed in the time range 2.5–2.0 Ga

[1]Pós-Graduação em Geodinâmica e Geofísica, Departamento de Geologia, Universidade Federal do Rio Grande do Norte – Natal (RN), Brazil. E-mails: zorano.souza@ufrn.br, frederico.vilalva@ufrn.br

[2]Instituto de Geociências, Universidade de Brasília – Brasília (DF), Brazil. E-mail: elton@unb.br

[3]Instituto de Geociências, Universidade Estadual de Campinas – Campinas (SP), Brazil. E-mail: elsonepo@unicamp.br

[4]Departamento de Geologia, Universidade Federal do Rio Grande do Norte – Natal (RN), Brazil. E-mail: rafael.motta@ufrn.br

[5]Université Blaise Pascal – Aubière, France;

[6]Pós-Graduação em Geodinâmica e Geofísica, Universidade Federal do Rio Grande do Norte – Natal (RN), Brazil. E-mail: samir.valcacio@gmail.com

[#]*In memoriam*.

*Corresponding author.

Supplementary data

Supplementary data associated with this article can be found in the online version:

Supplementary Tables A1–A3 (http://sfbjg.siteoficial.ws/Sf/2023/4889202320220079.pdf).

(Taylor and McLennan 1985, Santosh *et al.* 2015, Sun *et al.* 2019, Ganade *et al.* 2021). Hence, the Archean–Proterozoic transition has long been considered a marker of relevant changes in the geothermal gradient that led to major formation of continental crust in the Archean and evolved to a regime of progressively lower geothermal gradient and dominance of crustal recycling in the Middle and Late Proterozoic (Taylor and McLennan 1985, Martin 1994, Laurent *et al.* 2014, Nebel *et al.* 2018).

The Borborema Province in northeastern Brazil (Almeida *et al.* 1981) presents an outstanding opportunity to study the Neoarchean–Paleoproterozoic transition. This territory is located at the margin of a large continental landmass formed during the amalgamation of the Congo and São Francisco cratons (inset in Fig. 1). This vast region comprises Paleo-to Neoproterozoic units and some Archean fragments, the last ones represented by the São José do Campestre, Campo Grande, Granjeiro, Tróia, Mombaça, and Cruzeta remnants (Neves 2003, 2011, Van Schmus *et al.* 2003, 2008, 2011, Dantas *et al.* 2004, 2013, Souza *et al.* 2007, Ferreira *et al.* 2020, 2021, Ganade *et al.* 2021).

In this article, we present new zircon U-Pb geochronological, whole rock, and microprobe data for the São José do Campestre granite complex (Fig. 1) and discuss the following topics:

I. the evolution mechanism of a Late Neoarchean granite;
II. the magma genesis and associated tectonics;
III. the relative role of upper mantle and lower crustal materials as sources of magmas at that time.

GEOLOGICAL SETTING

The Borborema Province comprises several metasupracrustal sequences overlying Archean to Paleoproterozoic gneissic basement that have been subsequently intruded by several plutons during the Late Neoproterozoic (Figs. 1 and 2). This province resulted from the convergence of the West Africa — Amazonian and São Francisco — Congo cratons during the assembly of West Gondwana and extends from central and northeastern Brazil to the Trans-Saharan Orogen in northwestern Africa (Tuareg and Benino-Nigerian shields) and the Central African Orogen of Cameroon, Chad, and the Central African Republic (Caxito *et al.* 2020). All units forming this province are controlled and/or reworked by a complex system of continental-scale high-temperature shear zones (Caby *et al.* 1991, Vauchez *et al.* 1995, Neves *et al.* 2021).

The São José do Campestre Massif (SJCM; Fig. 3) comprises:

I. an Archean complex in its central part, which is composed of mafic to felsic metaplutonics and metasupracrustals;
II. Paleoproterozoic orthogneisses (the Caicó Complex; 2.25–2.11 Ga) surrounding the Archean core;
III. late Neoproterozoic metasupracrustal sequences (the Seridó Group with detrital zircons with age ≥ 640 Ma);
IV. voluminous Pan-African granitoids and pink granite dykes (zircon U-Pb ages ranging from 600 to 543 Ma) (Dantas 1996, Van Schmus *et al.* 2003, Dantas *et al.* 2004, 2013, Hollanda *et al.* 2011, Souza *et al.* 2016, Ferreira *et al.* 2021).

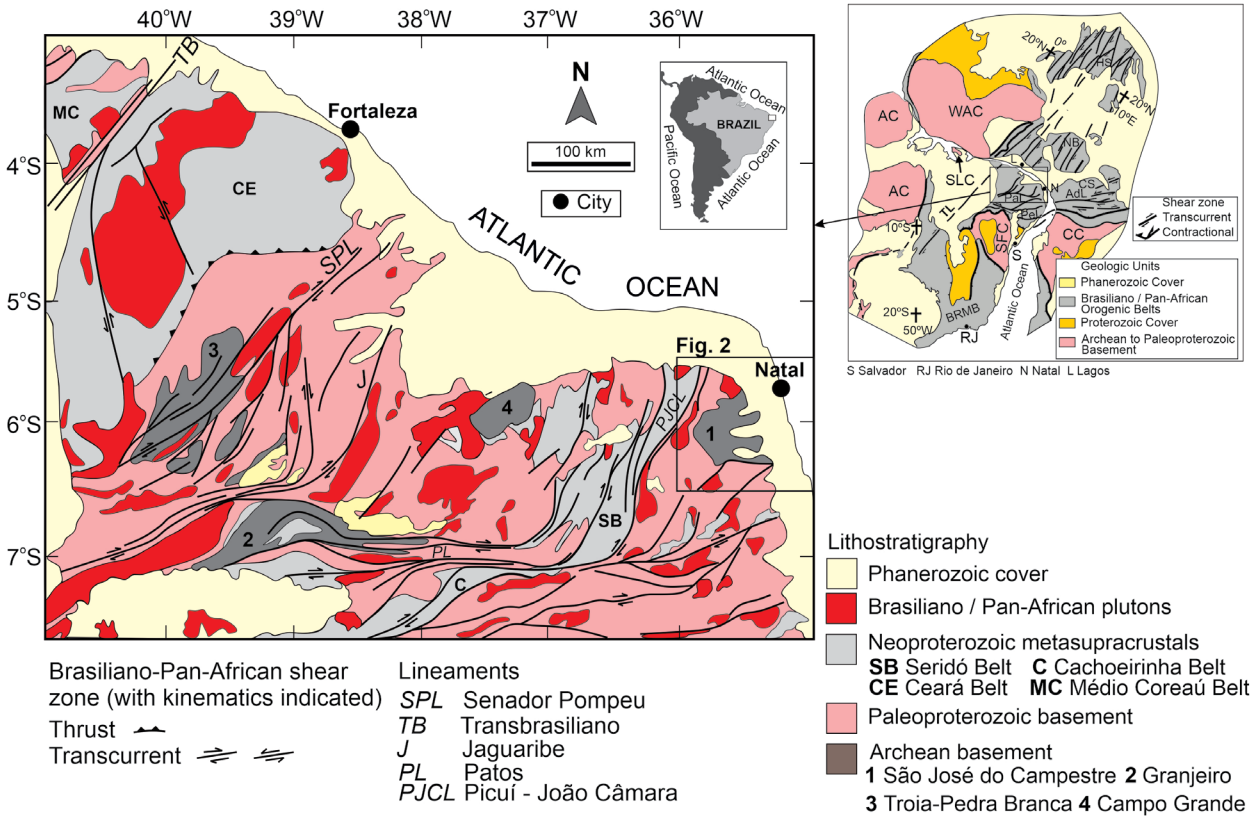

WAC - SLC: West Africa - São Luís Craton; AC: Amazonian Craton; SFC: São Francisco Craton; CC: Congo Craton; BRMB: Brasília and Ribeira Mobile Belts; CS: Cameroon Shield; NB: Nigerian Belt; HS: Hoggar Shield; TL: Transbrasiliano Lineament; PaL: Patos Lineament; PeL: Pernambuco Lineament; AdL: Adamaoua Lineament.

Figure 1. Simplified geology of the northern portion of the Borborema Province (integrated after Angelim *et al.* 2004, Arthaud *et al.* 2008, Souza *et al.* 2016, Oliveira and Medeiros 2018, Ganade *et al.* 2021). Inset shows the study region in a pre-drift reconstruction (after Sá 1994).

The SJCM Archean complex is composed of the following units (Dantas 1996, Dantas *et al*. 2004, 2013, Souza *et al*. 2016, Ferreira *et al*. 2020): Senador Elói de Souza complex — diopside-grossular-bearing anorthosite, garnet-bearing metagabbro, and garnet-bearing paragneiss (3.03 Ga); São Pedro do Potengi biotite-bearing granodiorite (3.12 Ga); Brejinho complex — gabbro to tonalite metaplutonics (3.18 Ga); Serra Caiada biotite ± hedenbergite ± hornblende-bearing granitic orthogneiss (3.36 Ga); marbles and paragneisses of unknown age (inherited zircons of 3.4 and 3.2 Ga, and metamorphic zircon of ~3.0, 1.9, and 0.58 Ga); and Bom Jesus metagabbro to quartz diorite to tonalite gneisses (c. 3.41 Ga). Ediacaran plutons and N-S trending granite dykes are the last Precambrian magmatic events in the region.

Late Neoproterozoic high-temperature shear zones (Picuí-João Câmara Shear Zone) juxtapose the SJCM and the Rio Piranhas-Seridó Domain, which is composed of Neoproterozoic metasedimentary rocks (Seridó Group) overlying a Paleoproterozoic basement (Caicó Complex). Late Ediacaran structures are westward plunging synforms and antiforms in the western side of the Archean block and a southern plunging inverted antiform in the southern portion (Viegas 2007, Viegas and Souza 2007).

The São José do Campestre granite complex (SJCgr) is a hornblende-biotite-bearing granite with subalkaline and metaluminous affinity, previously analyzed by TIMS (zircon U-Pb), which yielded ages of 2685 ± 9 Ma (n = 6, MSWD of 8.8) and 2655 ± 4 Ma (n = 6, MSWD of 0.28), and whole rock Nd model ages of 3.5–3.3 Ga with $\varepsilon_{Nd}(t)$ between –4.2 and –6.2 (Dantas 1996, Dantas *et al*. 2004). The SJCgr has been interpreted as derived from the melting of either earlier gneisses (Dantas 1996, Dantas *et al*. 2004) or an enriched mantle in a subduction tectonic setting (Dantas *et al*. 2013, Souza *et al*. 2016).

FIELD GEOLOGY

The São José do Campestre granite (SJCgr) crops out in the southern limit of the SJCM near the city of São José do Campestre, with the northern and eastern limits nearby Santa Maria and Boa Saúde cities, respectively (Fig. 2), in the Rio Grande do Norte state. It is a holocrystalline, medium- to coarse-grained, equigranular to slightly inequigranular, gray to pink deformed granite (Figs. 3A and 3B). A prominent subhorizontal lineation (Lγ) with a WSW-ENE trend is marked by the orientation of hornblende + biotite + K-feldspar + magnetite. Late millimetric to centimetric size magnetite + K-feldspar ± biotite-rich veins crosscut (Figs. 3A and 3C) or follow the linear fabric (Fig. 3B).

Hornblende-rich quartz diorite occurs as autoliths or in interdigitated contacts with the host granite (Figs. 3C and 3D). Incomplete mixing of granite and quartz diorite occurs in some places (Fig. 3E). Igneous layering (Sγ) is characterized by alternate layers of biotite-bearing pegmatite and hornblende-biotite-bearing tonalite crosscutting an earlier magmatic linear fabric (Lγ) of the hosting SJCgr, and both units are overprinted by a NW-SE tectonic planar fabric S_1 (Fig. 3F).

METHODS AND ANALYTICAL TECHNIQUES

Analytical methods included classical field and petrographic descriptions, as well as additional whole rock and mineral chemistry for selected SJCgr samples. These data were integrated with former results from Viegas (2007), Dantas *et al*. (2013), Souza *et al*. (2016), and Ribeiro (2019).

Microprobe analyses of selected amphibole, biotite, plagioclase, microcline, and Fe-Ti oxide crystals were done on a Cameca SX50 electron microprobe hosted at the Geosciences Institute, Universidade de Brasília (UnB). Analytical conditions were 15 kV of accelerating voltage, a beam current of 25 nA, a 10 s counting time, and a spot size of 1 μm. In-house standards included synthetic and natural minerals. Amphibole structural formula, Fe^{2+}/Fe^{3+}ratio, and (OH) calculations were done with the spreadsheet of Locock (2014), according to the IMA nomenclature scheme (Hawthorne *et al*. 2012). Cation proportions for biotite and feldspars were computed based on 24 and 8 oxygen molecules, respectively (Deer *et al*. 2013). Fe-Ti oxides were computed for 4 oxygen molecules/3 cations and Fe_2O_3 and FeO from charge balance after Carmichael (1967). For the feldspars and biotite, all iron was assumed as FeO. The analytical errors are ± 0.5–2% for SiO_2, Al_2O_3, Fe_2O_3, MgO, MnO, CaO, and TiO_2 and 4.5–5.6% for Na_2O and K_2O. All microprobe results are reported in Suppl. Data Table 1.

A selected sample (CLZ40) was analyzed for major and trace elements at ALS Minerals Laboratories (www.alsglobal.com). Major elements were measured by inductively coupled plasma atomic emission spectroscopy (ICP-AES), whereas trace element abundances were computed by inductively coupled plasma mass spectroscopy (ICP-MS) after fusion with lithium tetraborate. Loss on ignition (LOI) was determined by the gravimetric method after 1 h of heating at 1,000°C. The analytical errors are < 7% for oxides and < 6% for trace elements. Other 14 whole rock analyses were compiled from Dantas *et al*. (2013). Supplementary Data Table 2 displays all whole-rock chemical data.

For *in-situ* zircon U-Pb dating, one sample (ES471) was fragmented with a jaw crusher, followed by 250 mm grinding, manual panning, and mineral separation by methylene iodide and a Frantz magnetic separator. Zircon grains were then manually selected with a binocular loupe, mounted on epoxy resin, and imaged by cathodoluminescence. All procedures were conducted at the Geoscience Institute of the Universidade Estadual de Campinas (IG/UNICAMP). The isotopic data were also obtained at IG/UNICAMP on an ICP-MS Element XR (Thermo Scientific) coupled to an Excite193 laser ablation system (Photon Machines) with a HelEx ablation cell (25 μm laser beam). Data were reduced with the Iolite software and compared with the reference zircon 91500 (1065.4 ± 0.3 Ma; Wiedenbeck *et al*. 1995) and the Peixe zircon (571 ± 10 Ma; Navarro *et al*. 2017) for data quality control. Supplementary Data Table 3 reports all zircon U-Th-Pb isotopic results.

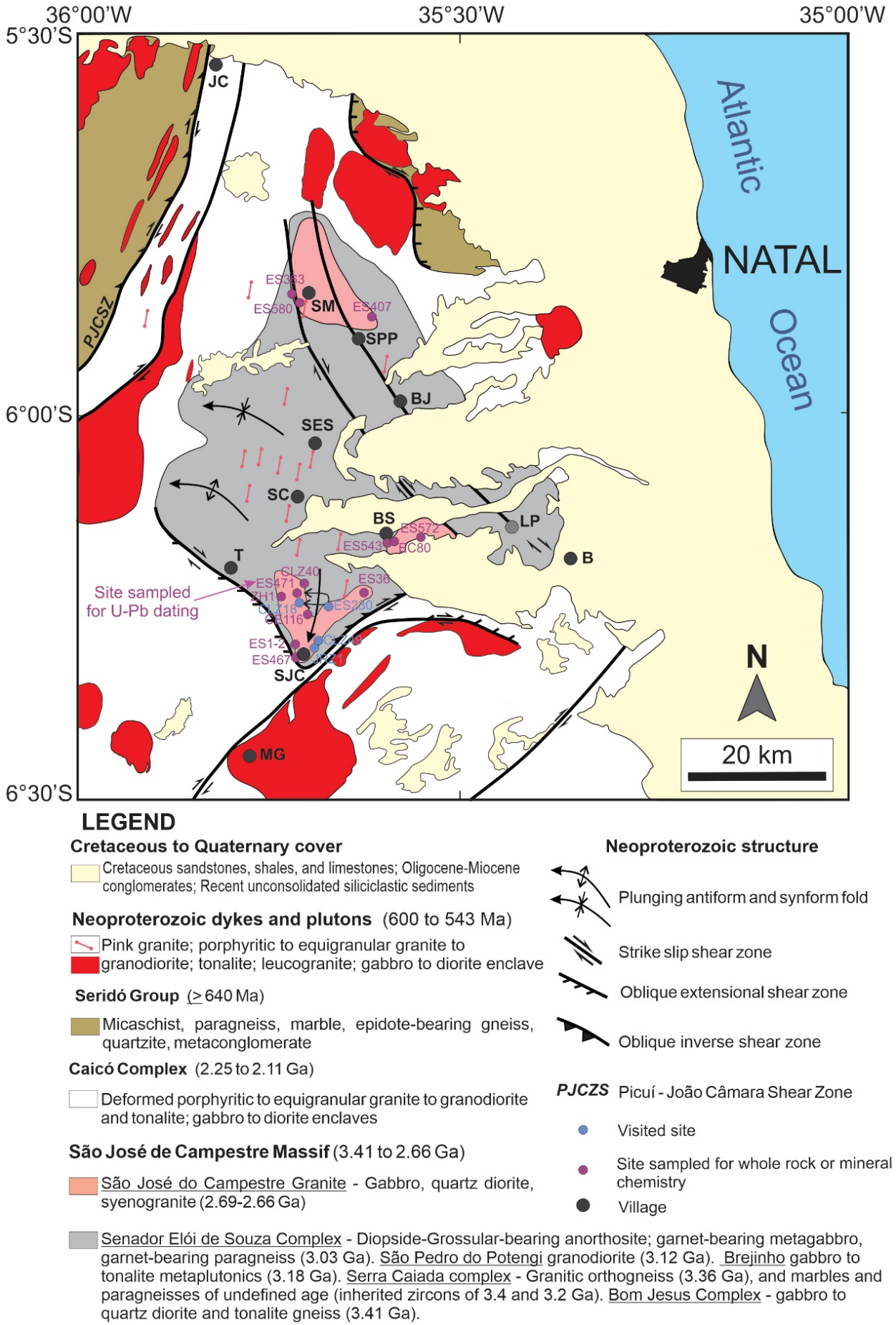

B: Brejinho; BJ: Bom Jesus; BS: Boa Saúde; JC: João Câmara; LP: Lagoa de Pedras; MG: Monte das Gameleiras; SC: Serra Caiada; SES: Senador Elói de Souza; SJC: São José do Campestre; SM: Santa Maria; T: Tangará.

Source: modified from Viegas (2007), Viegas and Souza (2007), Souza and Dantas (2008), Dantas *et al.* (2004, 2013). Zircon U-Pb ages after Dantas (1996), Dantas *et al.* (2004, 2013), and Souza *et al.* (2016).

Figure 2. Simplified geologic map of the study area.

RESULTS

Petrography

The SJCgr rocks vary from quartz diorites to syenogranites (Streckeisen 1976), the latter being the main litotype, with variable modal contents of felsic minerals. According to Dantas *et al.* (2013), the modal composition of the SJCgr follows the calc-alkaline intermediate K-enrichment trend of Lameyre and Bowden (1982).

On textural grounds, these rocks present equigranular, medium-grained textures, and a discrete alignment of hornblende (Fig. 4A), which is usually anhedral and has a skeletal to poikilitic texture involving feldspar and quartz and late transformation to biotite (Figs. 4A–4D). Sodic, myrmekitic plagioclase ($An_{10–25}$ by the Michel-Lévy method), perthitic to mesoperthitic microcline (Fig. 4C), and quartz often show minor evidence of late recrystallization. This includes earlier-formed crystals showing irregular shapes and subhedral

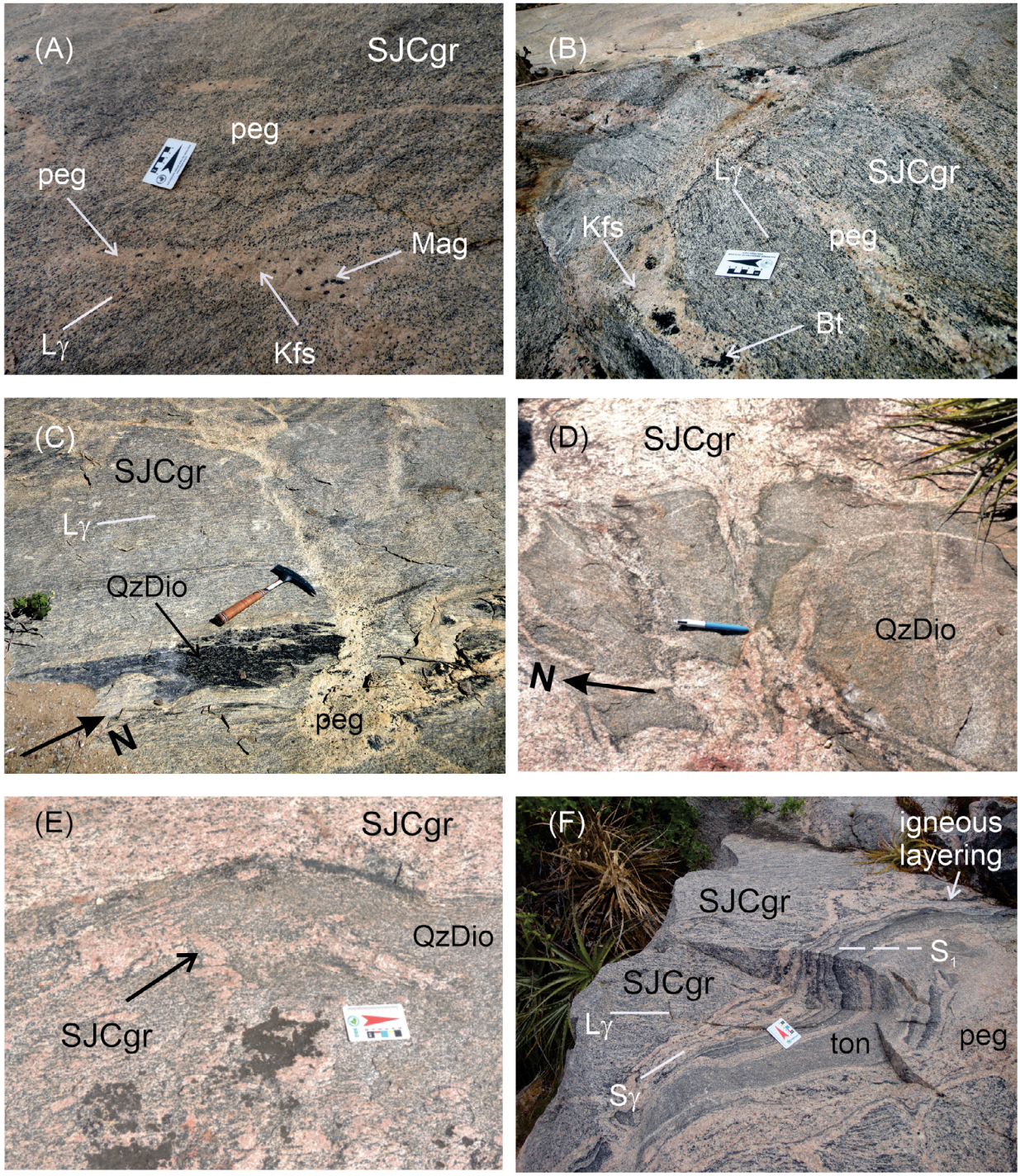

SJCgr: São José do Campestre granite; QzDio: Quartz diorite; ton: Tonalite; peg: Pegmatite; Sγ/Lγ: magmatic planar/linear fabric; S_1: tectonic fabric.

Figure 3. Field aspects of the São José do Campestre granite complex, NE Brazil. (A) SJCgr crosscut by late hololeucocratic magnetite-rich pegmatite. (B) Gray SJCgr with late biotite-rich pegmatite injected along the linear fabric defined by the orientation of hornblende + recrystallized K-feldspar. (C) Quartz diorite interleaved with granite. (D) SJCgr with quartz diorite autolith. (E) Incomplete mixing of granite and quartz diorite. (F) SJCgr crosscut by late interlayered pegmatite and leucotonalite (below the scale). (A, B, and C) Site ES1-2, São José do Campestre city (6.308°S/35.715°W). (D, E, and F) Site ES580, Santa Maria city (5.854°S/35.701°W). Abbreviations for minerals (Whitney and Evans 2010): Kfs K-feldspar; Bt: Biotite; Mag: Magnetite. All pictures display horizontal surface.

polygonal mosaics. Quartz appears interstitial to feldspar grains or forms discontinuous millimetric-size venulations concordant with the magmatic fabric.

Mafic phases (up to 65% in volume) are composed mainly of deep green to brown hornblende (poikilitic grains enclosing microcline, plagioclase, and zircon; up to 2–3 mm in size; Figs. 4C and 4D), plus brown biotite (< 1–5%; usually related to alteration of hornblende; locally, it may be altered to green chlorite + titanite + magnetite) and magnetite (< 1–3%; irregular, skeletal to interstitial grains up to 4 mm in length). Hornblende predominates in the less evolved quartz dioritic facies, whereas biotite surpasses hornblende in the most evolved ones.

Other accessory phases include apatite (< 1% in the syenogranites and up to 3% in quartz diorites; euhedral to rounded crystals; Fig. 4C), titanite (< 1–2%; anhedral grains replace biotite), allanite (< 1%; anhedral crystals with epidote rim and cross-cutting earlier feldspar and biotite; it may reach up to 2 mm in

Table 1. Major and trace element fractional crystallization modeling of the Neorchean São José do Campestre granite complex, NE Brazil.

	Group 2 – Enriched LREE and HREE				**Group 3 – Less enriched LREE and flat HREE**			
	C_0	**C_{L2}**	**C_{L2}'**	**Cumulate C_2**	**C_0**	**C_{L3}**	**C_{L3}'**	**Cumulate C_3**
	ES467	**ES572**	**FC = 40%**	**Σr^2 = 0.31**	**ES471**	**CE116B**	**FC = 15%**	**Σr^2 = 0.02**
SiO_2 (wt. %)	59.70	66.19	66.23	49.82	69.89	74.10	74.11	48.15
TiO_2	0.90	0.54	0.57	1.40	0.53	0.28	0.29	1.75
Al_2O_3	15.87	17.70	17.60	13.26	13.40	12.56	12.57	17.73
Fe2O3	6.96	3.09	3.12	12.77	5.38	3.16	3.16	16.83
MnO	0.10	0.04	0.05	0.18	0.09	0.04	0.08	0.14
MgO	4.30	1.39	1.39	8.68	0.31	0.19	0.19	0.93
CaO	6.62	4.44	4.45	9.91	1.70	0.99	0.99	5.33
Na_2O	4.12	4.28	4.71	3.23	3.01	3.28	3.26	1.75
K_2O	1.13	2.16	1.88	0.00	5.61	5.36	5.35	6.90
P_2O_5	0.30	0.17	0.00	0.74	0.08	0.05	0.00	0.50
Cs (ppm)	0.37	0.50	0.80		0.52	2.6	2.8	
Hf	4.99	5.3	11.0		12.5	11.5	12.2	
Nb	9.42	9.5	6.1		34.0	34.4	54.2	
Ni	96.30	17.4	6.0		2.79	2.4	0.01	
Rb	20.80	55.4	37.5		138.0	182.0	152.9	
Sr	628.0	540.9	610.2		104.0	68.1	41.2	
Ta	0.45	0.7	0.1		1.65	2.4	0.3	
Th	5.14	12.2	8.9		11.4	23.7	45.8	
U	0.23	0.6	0.5		1.36	4.3	8.1	
Y	22.7	10.5	23.0		87.9	75.0	182.0	
Zr	218.0	228.4	277.7		535.0	403.2	433.3	
Cumulate (wt. %)				Ol Gabbro-norite				Ol monzonite
Plagioclase (An_{38})				49.38				30.55
K-feldspar (Or_{92})								42.06
Hortonolite (Fo_{30})				19.11				6.25
Orthopyroxene (En_{90})				7.59				
Dio-Hed (Wo_{50-43})				19.43				
Hornblende								7.75
Magnetite								9.09
Ilmenite				2.73				3.10
Apatite				1.76				1.18
Zircon								0.02

LREE: light rare earth element; HREE: heavy rare earth elements; C_0 and C_L: less evolved and most evolved samples, respectively; C_L': calculated liquid after extraction of the cumulate; Σr^2: statistical error adjustment of the theoretical model through matrix inversion; FC: % of fractional crystallization. K-feldspar, amphibole, magnetite, and ilmenite compositions used in modeling fractional crystallization are from this article. The other phases were compiled from Deer *et al.* (2013). The partition coefficients used for modeling are mostly those compiled by Nielsen (2022). We also used partition coefficients for zircon after Martin (1987), Thomas *et al.* (2002), Rubatto and Hermann (2007), Burnham and Berry (2012), and Gudelius *et al.* (2020), and apatite after Prowatke and Klemme (2006). Symbols for minerals (according to Whitney and Evans 2010): Ol: olivine; Di: diopside; Hd: hendebergite; An: anorthite; Wo: wollastonite; Fo: forsterite; En: enstatite; Or: orthoclase.

diameter), garnet (< 1%; irregular rounded grains associated with plagioclase), zircon (euhedral to subhedral, quadratic to rectangular-shaped gray grains crosscutting or hosted in hornblende or magnetite; it may reach up to 0.5 mm in length; Fig. 4B), and rare relicts of uralitized pale green diopside.

All analyzed samples show a marked fabric defined by continuous millimetric thick bands of feldspar plus quartz alternated with mafic-rich bands (*cf.* Figs. 3A to 3F). A new generation of hornblende postdates earlier poikilitic hornblende, and features of recrystallization of plagioclase and microcline point to the overprinting of magmatic minerals and fabrics.

Mineral chemistry

Electron microprobe analyses of feldspar (plagioclase, $n = 5$; K-feldspar, $n = 3$), amphibole ($n = 8$), biotite ($n = 4$), and oxides ($n = 2$) of sample ES36 (see location in Fig. 3) are given as a supplementary data file (Suppl. Data Table 1). The analyzed spots were located on the core and crystalline rims of plagioclase and amphibole, and on K-feldspar, biotite, and Fe-Ti oxide crystal cores.

Feldspar

Plagioclase is sodic and shows no significant chemical zoning between the core and rims, and the anorthite content of five single crystals ranges from 12.68 to 15.33% (average: 13.85 ± 0.92%). Microcline has the composition $Or_{92\text{-}71}Ab_{8\text{-}29}$; perthitic exsolutions for one grain are still more sodic ($Ab_{99}An_1$).

Amphibole

The two types of amphibole crystals are hastingsite and ferro-pargasite (Fig. 5A; cf. Hawthorne *et al.* 2012). They have Si contents between 6.206 and 6.325 cations per formula unit (cpfu), Al between 1.937 and 1.997 cpfu, and Na+K between 0.839 and 1.003 cpfu. They are relatively homogeneous from core to rim, have low Ti contents (0.163–0.248 cpfu), and are Fe-enriched, with the fe# number [Fe/(Fe + Mg)] ranging from 0.90 to 0.91.

Biotite

Biotite crystals are relatively enriched in Ti (0.484–0.548 cpfu), Fe (4.88–4.958 cpfu), and Mg-depleted (0.573–0.646 cpfu), leading to fe# ratios between 0.89 and 0.9, which put them between annite and syderophyllite (Rieder *et al.* 1998, Deer *et al.* 2013; Fig. 5B). They plot within the 'primary biotite' field in the diagram after Nachit *et al.* (2005; Fig. 5C) and show chemical signatures like those found in micas of alkaline to slightly subalkaline magmas (Stussi and Cuney 1996; Fig. 5D).

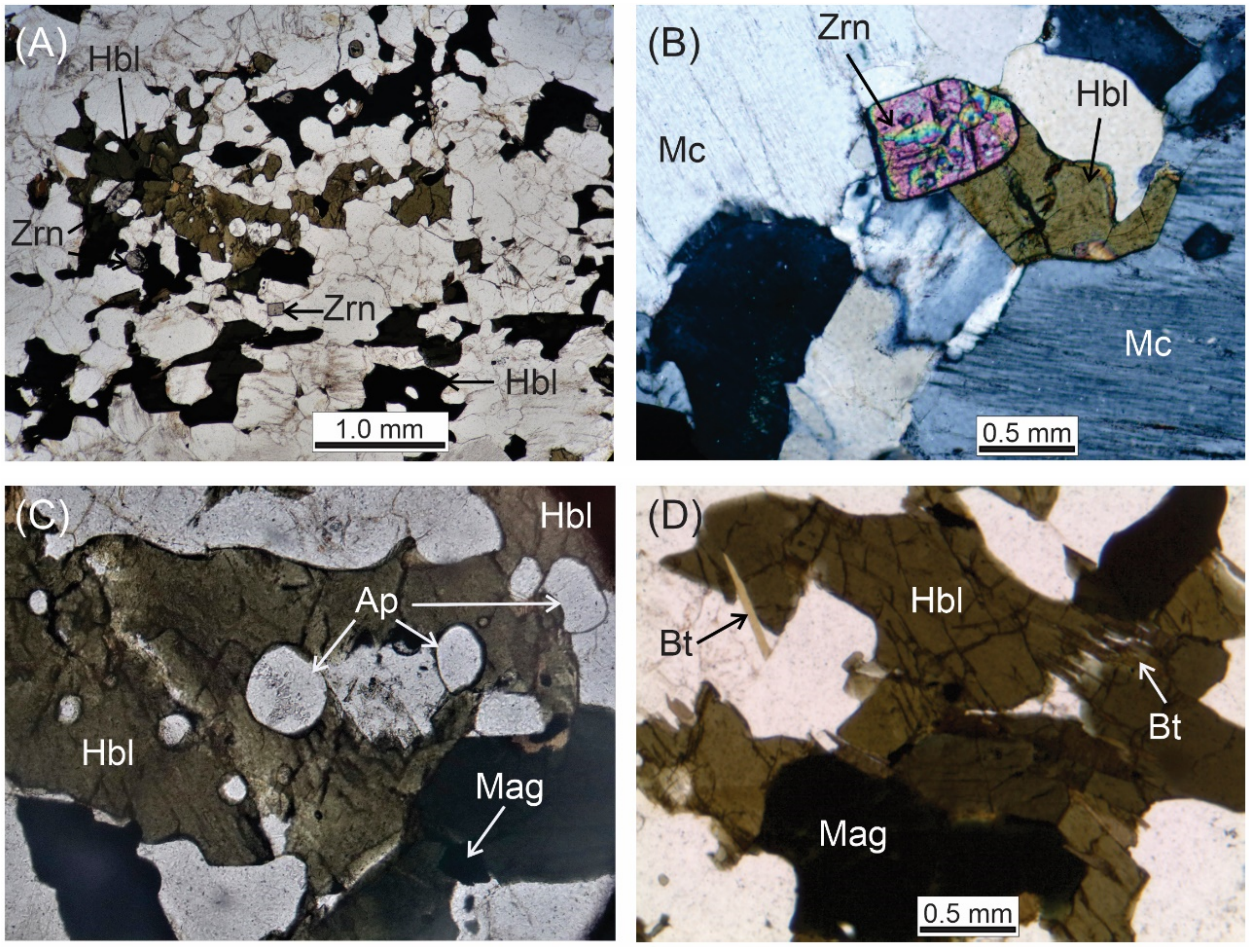

Figure 4. Petrographic and textural features (sample ES471; 6.236°S/35.710°W). (A) Green hornblende, apatite, zircon, and a colorless medium-grained quartz-feldspathic groundmass. (B) Mesoperthitic microcline, green hornblende, and zircon. (C) Detail of cumulate texture of hornblende and rounded apatite. (D) Detail of cumulate texture of hornblende and magnetite and late biotite lamella. Abbreviations for minerals (Whitney and Evans 2010): Mag: magnetite; Zrn: zircon; Hbl: hornblende; Mc: microcline. (A, B, and C) uncrossed polarizers; (D) crossed polarizers.

Iron oxides

Representative electron microprobe data of two oxide crystals indicate magnetite (TiO_2 0.94 wt. %, Al_2O_3 0.32 wt. %) and ilmenite (TiO_2 48.37 wt. %, FeO_t 47.51 wt. %, MnO 1.27 wt. %) with contents of the ulvöspinel molecule of 2.33 and 1.55, respectively.

Whole rock chemistry

Geochemical characterization

The analyzed samples were divided into three groups as follows (see Suppl. Data Table 2):

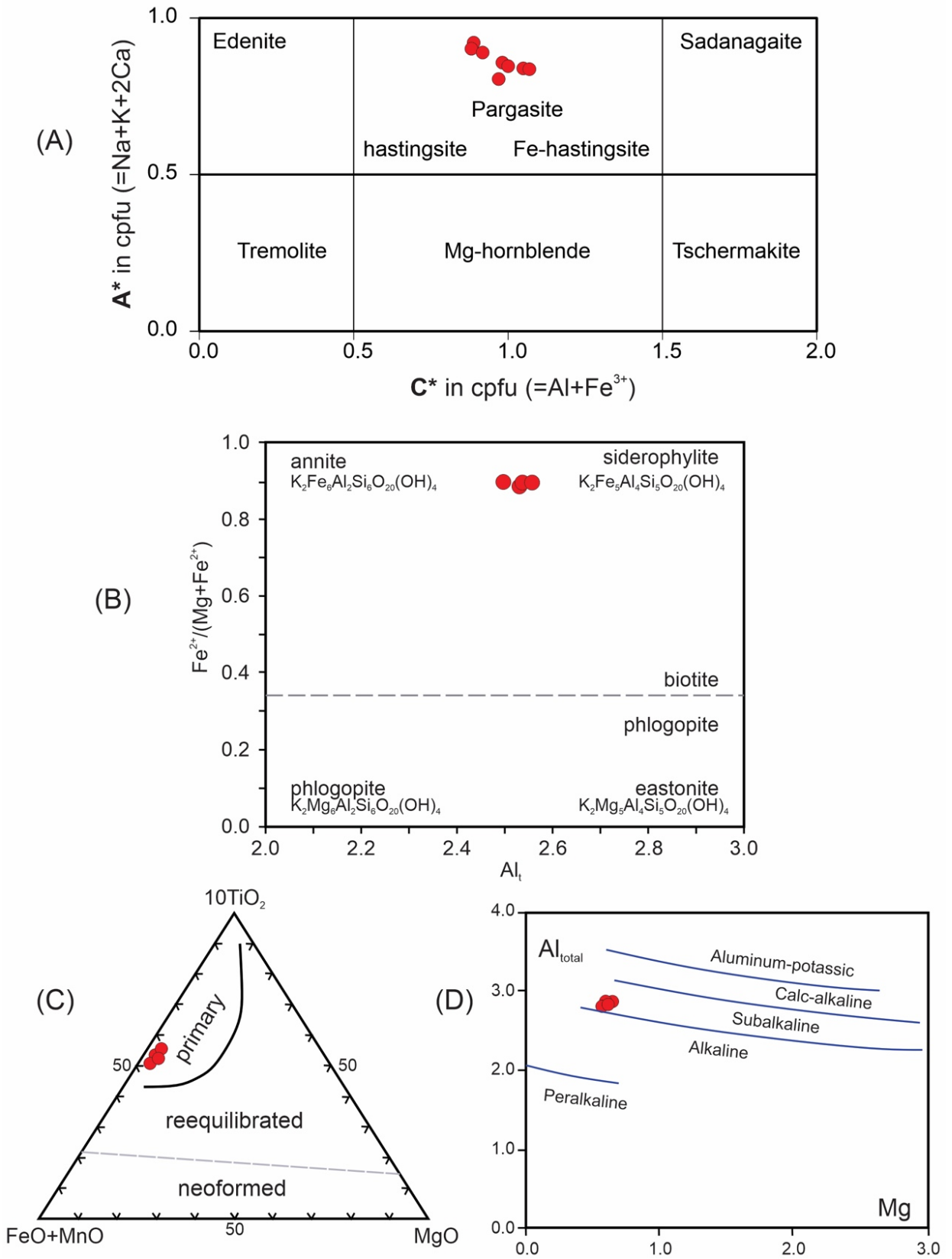

Figure 5. Mineral chemistry of amphibole (A) and biotite (B–D) according to different classifications. (A) C* (cpfu) vs. A* after Hawthorne *et al.* (2012). (B) Al_t (cpfu) vs. $Fe^{2+}/(Mg + Fe^{2+})$ after Rieder *et al.* (1998) and Deer *et al.* (2013). (C) Ternary plot TiO_2-(FeO + MnO)-MgO (all in wt. %) after Nachit *et al.* (2005). (D) Mg vs. Al_{total} (both in cpfu) of biotite from magmas of peralkaline to aluminum-potassic affinity after Stussi and Cuney (1996).

I. group 1 ($n = 1$) is the least evolved, with SiO_2 = 52.83 wt. %, and MgO = 5.35 wt. %, has the highest anorthite, diopside, and hypersthene and the lowest quartz and orthoclase normative contents;
II. group 2 ($n = 5$) with SiO_2 and MgO in the respective ranges of 58.49–67.8 wt. % and 3.64–0.57 wt. %;
III. group 3 ($n = 10$) with SiO_2 and MgO of 69.19–75.12 wt. % and 0.31–0.27 wt. %, respectively, and the highest quartz and orthoclase and the lowest anorthite and diopside normative contents.

Oxide composition (in wt. %) show that the SJCgr rocks have a wide SiO_2 variation (52.8–75.1); low TiO_2 (0.24–1.84) and P_2O_5 (0.05–0.29); and low-to-moderate MgO (0.10–5.35), CaO (0.84–9.02), Fe_2O_3t (2.45–8.96), and Al_2O_3 (11.7–15.55). They are moderately enriched in alkalis (Na_2O+K_2O of 4.5–8.6); less evolved samples (SiO_2 = 52.8–65.3) are Na-enriched (Na_2O/K_2O ratios of 2.0–3.6), whereas more evolved Si-rich facies (SiO_2 = 66.6–75.1) is K-enriched (Na_2O/K_2O ratios of 0.5–0.8). Fe_2O_3t contents are higher than MgO for individual samples, leading to Mg# [= 100MgO/(0.8998*Fe_2O_3t+MgO) molar] in the range of 3–55. All samples are silica-saturated, with normative quartz ranging from 2.8 to 35%.

Figure 6 exhibits major element plots (Barker and Arth 1976, Miyashiro 1978, Cox *et al.* 1979, Maniar and Piccoli 1989, Frost et *al.* 2001). In the TAS diagram (Fig. 6A), the samples are subalkaline (groups 1 and 2) or transitional to alkaline (group 3). This is corroborated by the SiO_2 vs. MALI plot (Fig. 6B), in which the samples scatter from calcic (the least evolved) to transitional to alkali-calcic (the most evolved). In the molar A/CNK vs. A/NK plot (Fig. 6C), which measures aluminum saturation, all samples are metaluminous. Coherently, in the ternary cationic diagram K-Na-Ca, the least evolved (group 1 and part of group 2) plot close to the trondhjemitic field, while the most evolved ones (part of group 2 and the entire group 3) tend to follow the calc-alkaline (K-enriched) trend or toward the Na-K edge (Fig. 6D).

In the *fe** vs. SiO_2 plot (Fig. 7A), less evolved samples show magnesian affinity, whereas the more evolved are ferroan (SiO_2 > 65 wt. %). They scatter within the I- to A-type granites (the

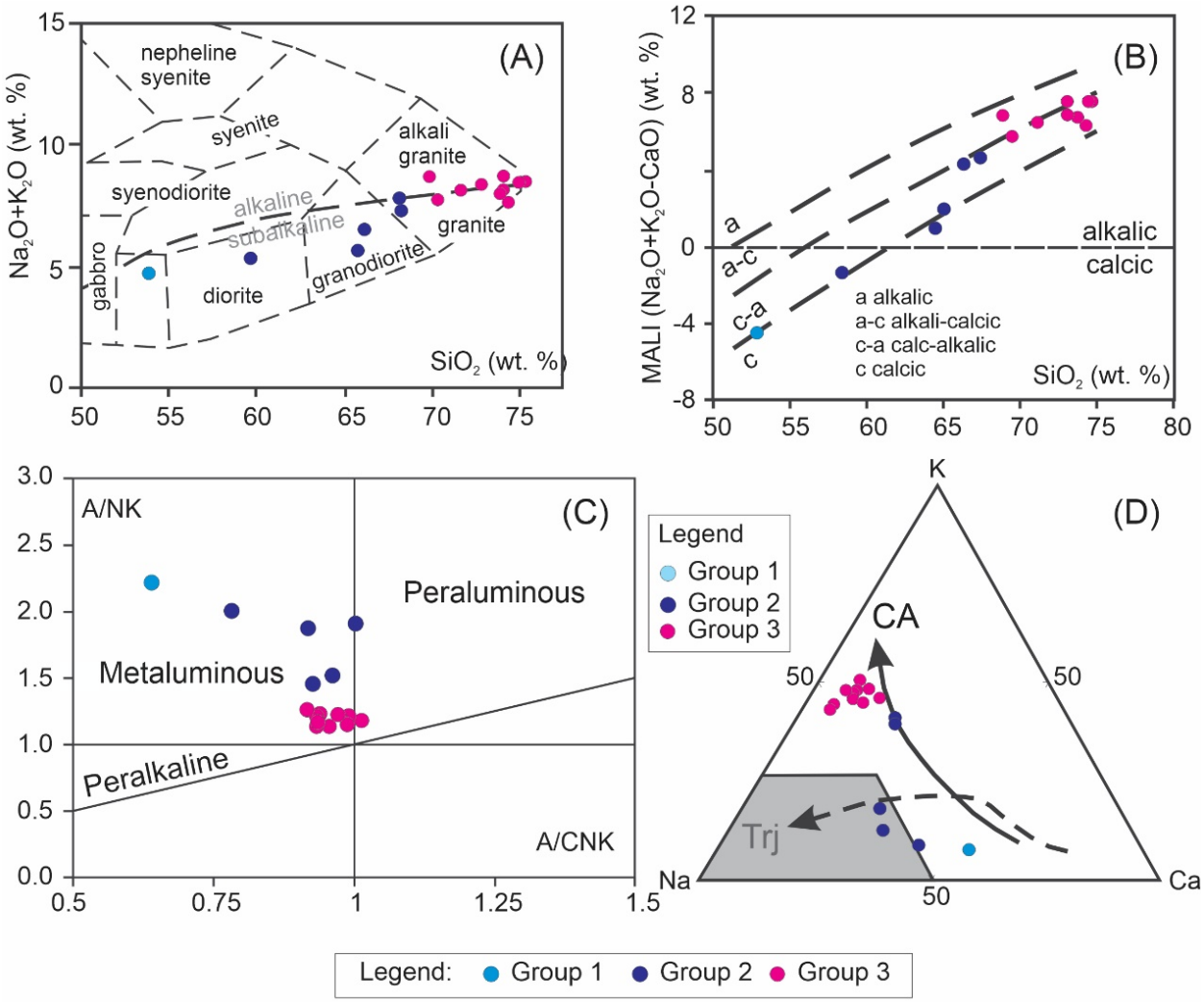

A: Al_2O_3; N: Na_2O; K: K_2O; C: CaO, all in molar proportion; MALI: Na_2O+K_2O-CaO in wt. %.

Figure 6. Major element geochemical characteristics of the studied rocks. (A) TAS (total alkalis vs. SiO_2 in anhydrous basis) diagram after Cox *et al.* (1979); alkaline-subalkaline boundary from Miyashiro (1978). (B) SiO_2 vs. MALI as proposed by Frost *et al.* (2001). (C) Saturation alumina index (Shand 1943) in the diagram of Maniar and Piccoli (1989). (D) Ternary cationic K-Na-Ca (Barker and Arth 1976) showing the classical calc-alkaline differentiation (labeled CA after Nockolds and Allen 1953) and trondhjemitic (named Trj from Barker and Arth 1976) trends; the trondhjemitic field is from Martin *et al.* (2005).

most evolved ones). In the *fe** vs. Al_2O_3 diagram (Fig. 7B), most samples have been classified from slightly oxidized to reduced A-type granite, while some less evolved samples are calc-alkaline. In the ternary plot ($NaO_2 + K_2O$)-5Fe_2O_3t-5(CaO + MgO) of Fig. 7C, these less evolved samples are akin to subducted and active continental margin related granites, whereas the most evolved correspond to A_2-type granites that are commonly associated with post-collisional geodynamic settings. In the bilogarithimic (Y + Nb) vs. Rb diagram (Fig. 7D), the studied rocks scatter within the post-collisional field of Pearce (1996).

Binary Harker-Type diagrams

Groups 1–3 as defined above show similar behavior for TiO_2, CaO, Fe_2O_3t, and P_2O_5 (Fig. 8) that decrease regularly with differentiation (i.e., increasing SiO_2). Al_2O_3 shares similar behavior, decreasing toward high silica, although the curve is less pronounced. Alkalis ($Na_2O + K_2O$) have opposite patterns as their abundances increase with differentiation. Of note, MgO content decreases strongly for group 2 but is very low (< 0.4 wt. %) and constant for group 3. Considering all samples, they define concave upward (for MgO) and concave downward (for K_2O) curves peaking at ~65 wt. % SiO_2. This may imply that magmatic evolution has been achieved by at least two main stages of crystallization (Wilson 1989).

Trace element data (Fig. 9) reveal lower Rb (< 33 ppm), Sc (25 ppm), Zr (72 ppm), and Ba (197 ppm) and high V (212 ppm) for group 1 ($n = 1$); group 2 ($n = 5$) has higher Sr (up to 685 ppm) and Ba (up to 4,588 ppm), with one sample having the highest Zr (910 ppm) and Nb (45.4 ppm); and group 3

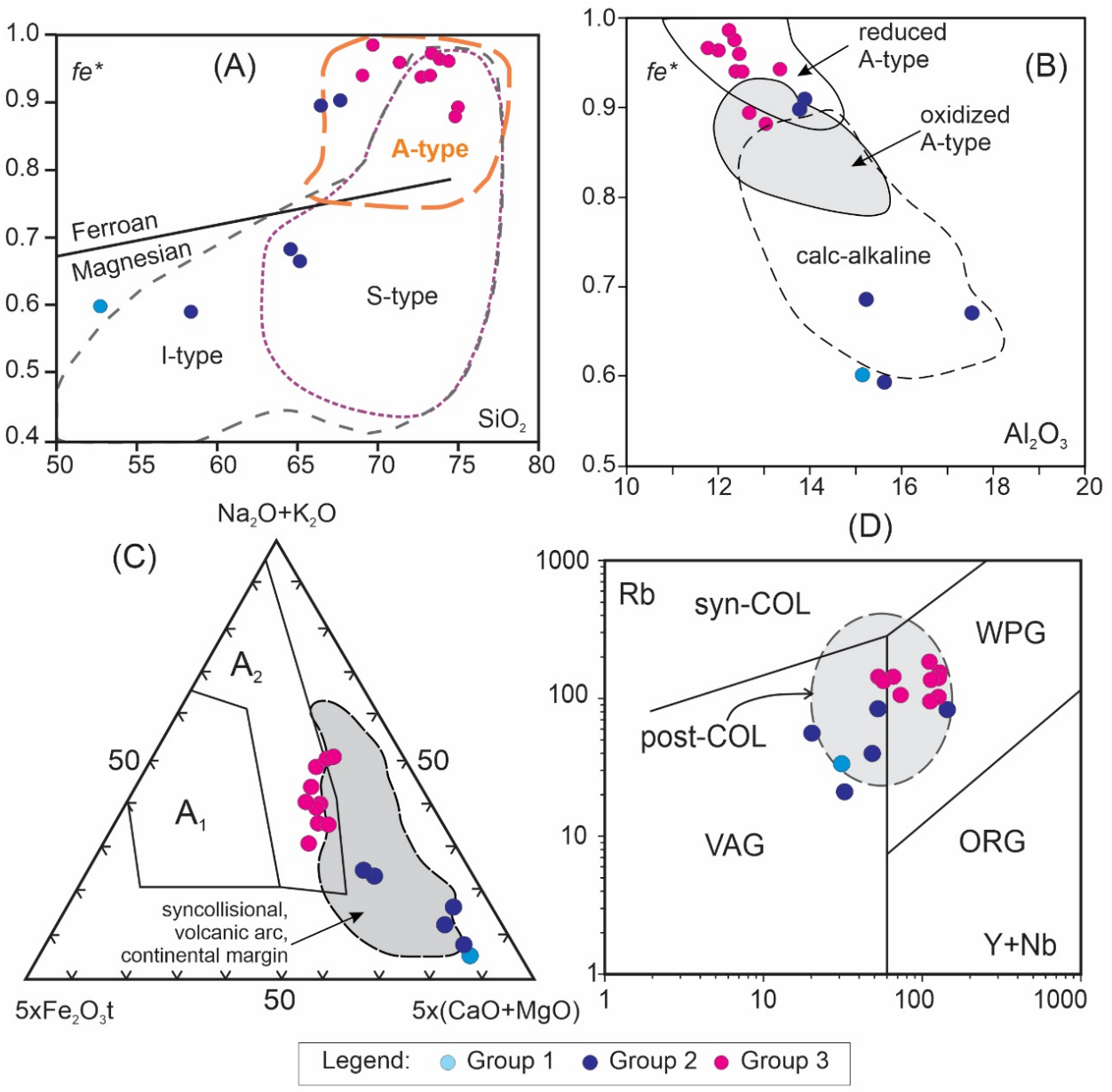

*fe**: FeOt/(FeOt + MgO); VAG: volcanic arc granitoid; syn-COL and post-COLL: syn- and post-collisional granitoid; WPG: within plate granitoid; ORG: ocean ridge granitoid; COL: collisional; A_1: silicic rocks of within plate settings (oceanic islands and continental rift); A_2: felsic igneous rocks of intracontinental and continental margin settings. FeOt, Fe_2O_3t, MgO, Al_2O_3, Na_2O, K_2O and CaO, in wt. %; Rb, Y, and Nb in ppm.

Figure 7. Geochemical affinity and tectonic setting of the studied rocks. (A) SiO_2 vs. *fe** and the fields of Ferroan, Magnesian, and I-, A- and S-type granitoids (Frost *et al.* 2001). (B) Al_2O_3 vs. *fe** and fields of calc-alkaline, oxidized A-type and reduced A-type granitoids (Dall'Agnol & Oliveira 2007). (C) (Na_2O + K_2O)-5Fe_2O_3t-5(CaO + MgO) ternary plot showing the fields of A_1- and A_2-type granites (Grebennikov 2014). (D) Bilogarithmic Y + Nb vs. Rb plot with the fields of volcanic arc, syn- and post-collisional, within plate, and ocean ridge granitoids (Pearce 1996).

(n = 10) has the highest Rb (182 ppm); Ni is usually low (< 40 ppm), except for one sample of group 1 and another one of group 3 (81.0–96.3 ppm). Figure 9 demonstrates the compatible behavior of V, Ni, and Sc, and the incompatible behavior of Rb and Ba in group 2. In group 3, Ba, Nb, Zr, and Sc behave as compatible elements, whereas Rb and Ni are incompatible.

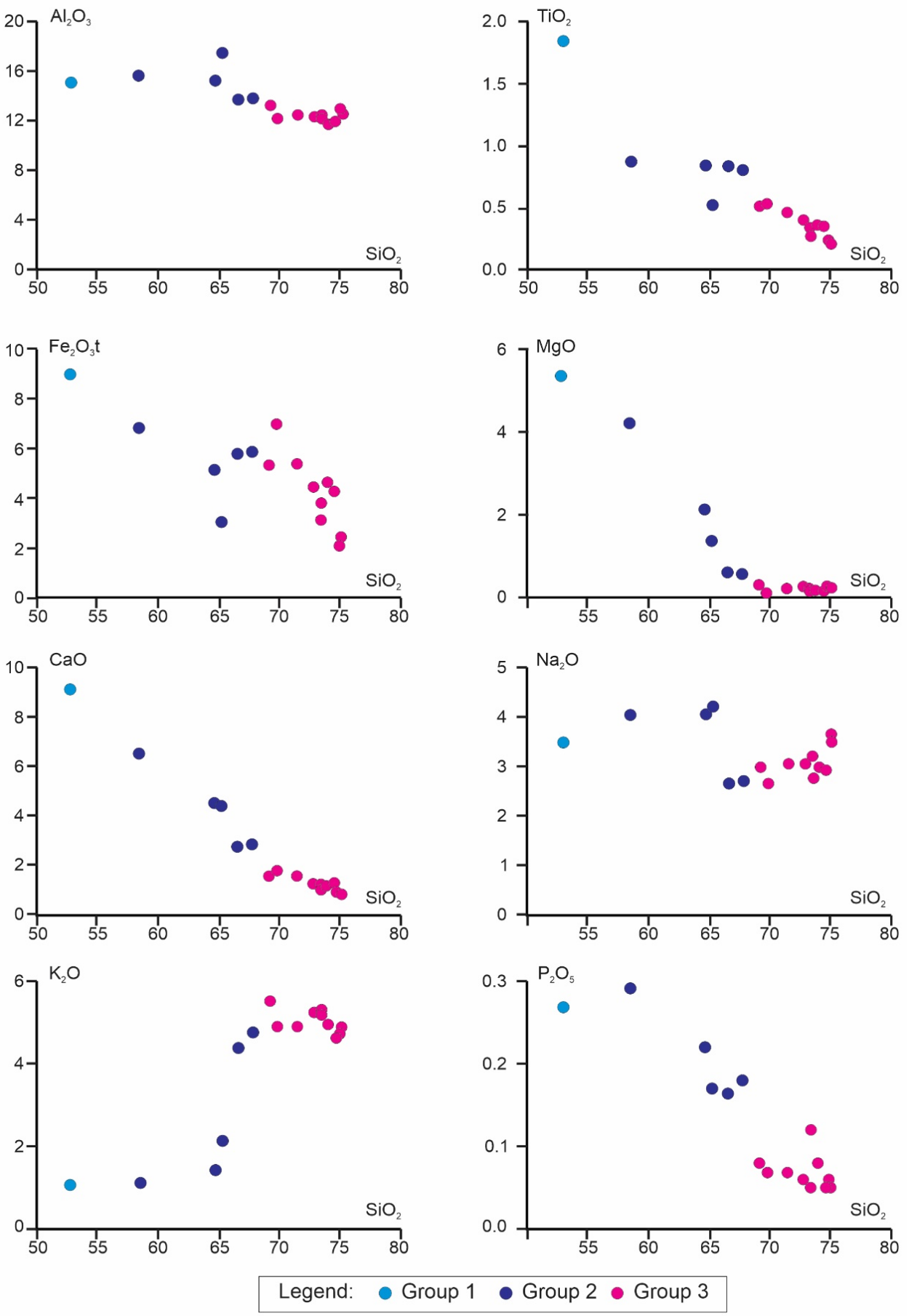

Figure 8. Major element Harker-type plots for the studied rocks (in wt. %).

Rare earth elements

The three rock groups exhibit discrete differences in their REE patterns and ratios, as follows. Group 1 (Fig. 10A) is enriched in light rare earth elements (LREE) with $(La/Yb)_N$ ratio of 3.45, has a slightly positive europium anomaly ($Eu/E^* = 1.32$), an almost flat heavy rare earth element (HREE) with $(Gd/Yb)_N$ of 1.3, and the lowest normalized Yb ($Yb_N = 11.0$). Its overall pattern is like those found in Archean enriched

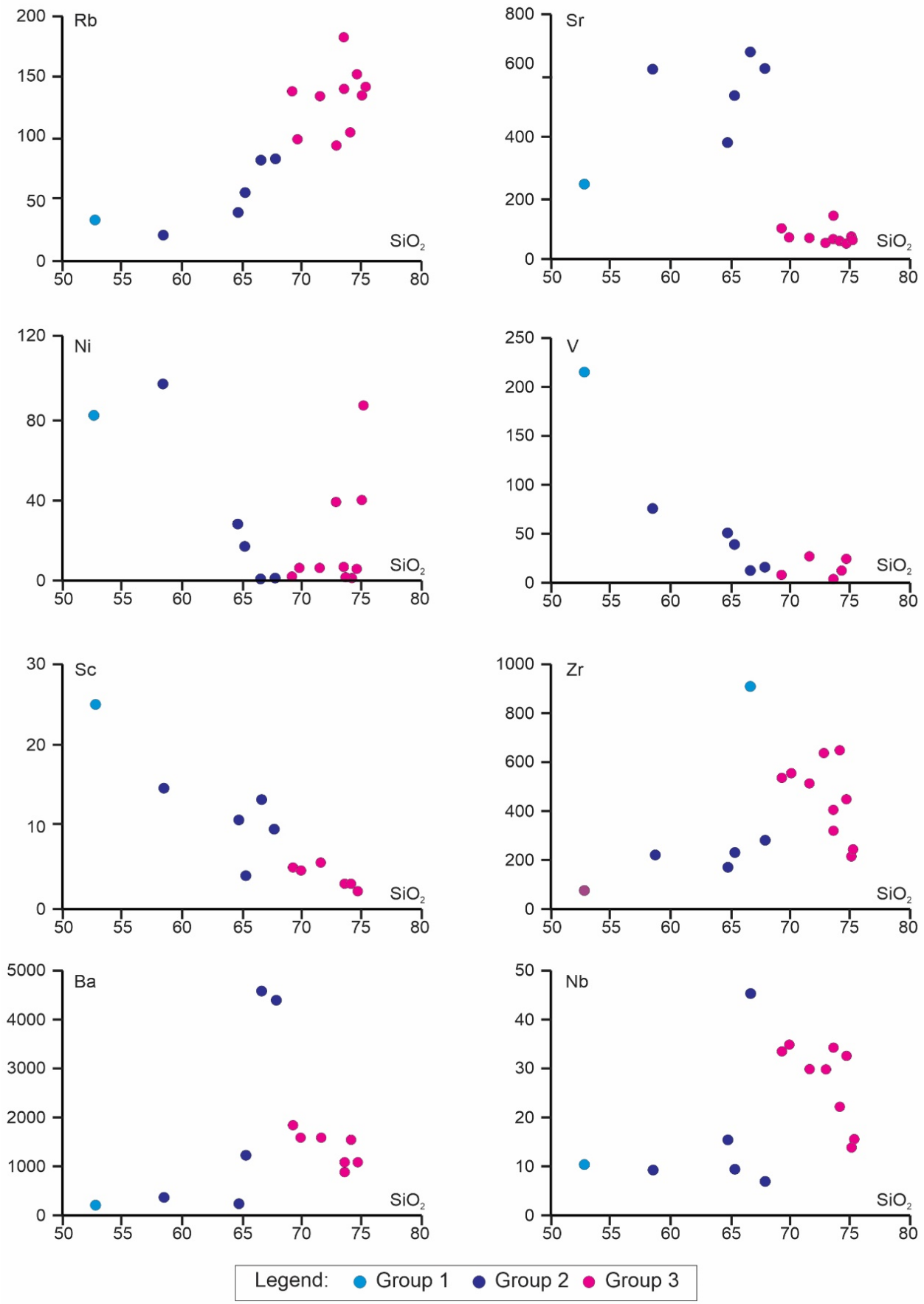

Figure 9. Trace element Harker-type plots for the studied rocks (SiO_2 in wt. %, and trace elements in ppm).

tholeiites (Condie 1976). Group 2 (Fig. 10B) has steeper LREE with $(La/Yb)_N$ of 29.5 ± 18.0, and less pronounced HREE [$(Gd/Yb)_N$ = 2.6 ± 1.0] patterns. There is no significant europium anomaly (Eu/Eu* = 0.91 ± 0.44) and the Yb_N varies around 21.2 ± 14.2. Such patterns are similar to those of Archean sanukitoids, which have $(La/Yb)_N$ = 41, Yb_N = 7.6, and Eu/Eu* = 0.84 (Martin *et al.* 2005, 2010, Heilimo *et al.* 2010). Group 3 (Fig. 10C) presents a fractioned trend from more-abundant LREE toward less-abundant HREE with (La/Yb)N = 7.0 ± 0.9 and the highest negative Eu anomaly (Eu/Eu* = 0.65 ± 0.14), as well as the highest Yb_N (43.2 ± 5.0). The Gd_N/Yb_N ratio (1.4 ± 0.1) is slightly lower than group 1. These REE patterns share similarities with modern arc granitoids, in which $(La/Yb)_N$ = 7.75, Yb_N = 21.8, and Eu/Eu* = 0.69 (Martin *et al.* 2010).

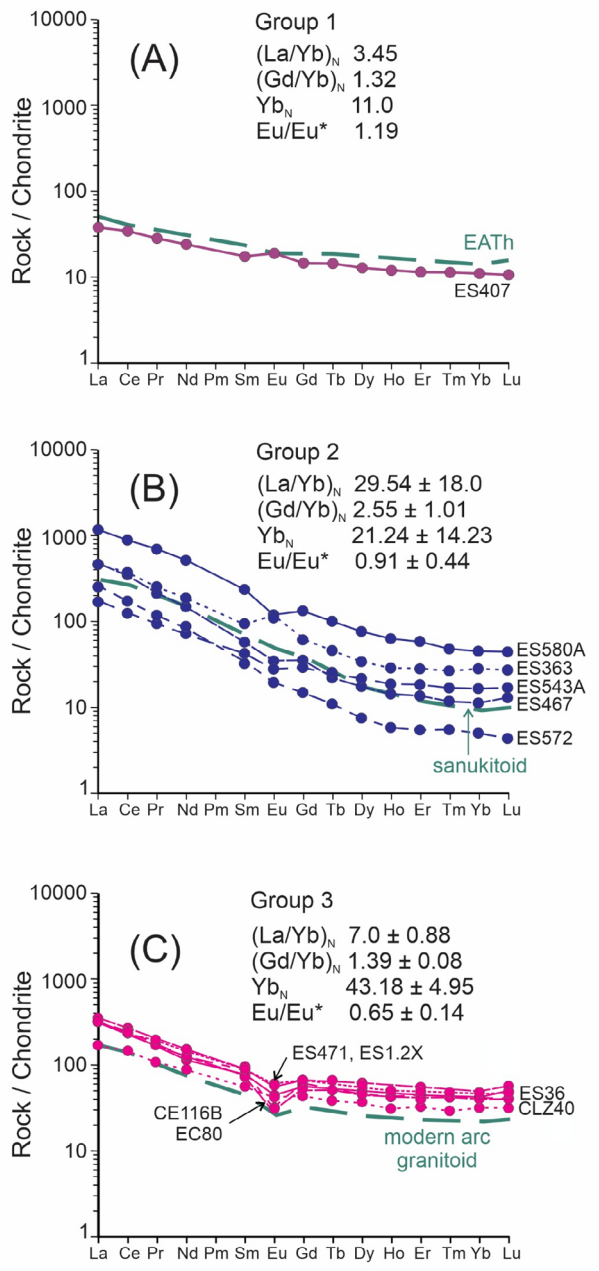

$(La/Yb)_N$: chondrite normalized (La/Yb); $(Gd/Yb)_N$: chondrite normalized (Gd/Yb); Yb_N: chondrite normalized Yb; Sm_N: chondrite normalized Sm; Eu_N: chondrite normalized Eu; Eu/Eu*: europium anomaly = $Eu_N/[(Sm_N + Gd_N)/2]$.

Figure 10. Chondrite-normalized (Sun and McDonough 1989) rare earth element patterns. (A) Group 1 sample ES407; average of enriched Archean Tholeiite (EATh) from Condie (1976). (B) Group 2 samples; average of late Archean sanukitoid from Martin *et al.* (2009). (C) Group 3 samples; average of modern arc granitoids from Martin *et al.* (2009).

Crystallization conditions

Pressure and temperature

Pressure estimates were obtained from the analyzed amphibole of sample ES36 (from group 3, as defined in the geochemical section) with the Amp-TB2 (Ridolfi 2021), an updated model for the amphibole-only barometer of Ridolfi and Renzulli (2012; equation P1e), and the amphibole/plagioclase Al-Si partitioning barometer of Molina *et al.* (2015). The first barometer yielded pressures from 497 to 601 MPa (average = 558 ± 28 MPa), whereas the formulation of Molina *et al.* (2015) gave slightly higher pressures in the range of 550–718 MPa (average = 636 ± 36 MPa), calculated using temperatures derived from the Amp-TB2 thermometer (see below) and an $An_{14}Ab_{84}Or_1$ oligoclase (within the plagioclase compositional range used in Molina's calibration). Altogether, it is assumed that the SJCGR has an average confining pressure of 597 ± 46 MPa. However, a word of caution is necessary when Fe-rich amphiboles are used for pressure calculations. Anderson and Smith (1995) argued that amphiboles with fe# [Fe/(Fe+Mg)] > 0.65 are indicative of low oxygen fugacity and yield overestimated pressures. Yang (2017) proposed an empirical method using CIPW normative quartz (Qtz) and albite (Ab) plus orthoclase (Or) compositions to estimate emplacement pressure of granite intrusions, referred to as Qtz-geobarometer (Yang *et al.* 2019, 2021). Using the improved Qtz-geobarometer of Yang *et al.* (2021), which corrects pressure estimation for both normative anorthite (following Blundy & Cashman 2001) and redox estate, most of the SJCgr samples (with normative quartz < 35 wt. %) cluster around 335 ± 124 MPa. Therefore, considering all pressure estimates, we assume that the emplacement of the SJCgr took place at pressures from ~400 to 600 MPa that corresponds to emplacement depths between ~15 and 23 km (for an average crustal density of 2.7 g/cm^3).

The apatite (TsatAp) and zircon (TsatZr) saturation thermometric expressions after Watson and Harrison (1983) and Harrison and Watson (1984), along with the Amp-TB2 amphibole-only thermometer (Ridolfi 2021), were used to estimate magmatic temperatures for the SJCgr. The TsatAp thermometer yielded the highest estimates of 958–868°C (average = 904 ± 28°C) that should approach the *liquidus* temperature. The TsatZr was applied to a group of ten samples with SiO_2 ranging from 69.19 to 75.12 wt. %, in which Zr (648–212 ppm) behaves as a compatible element (see whole rock composition in Suppl. Data Table 2). Results are slightly lower than TsatAp, varying from 812 to 913 (average = 870 ± 32°C). Amphibole crystallization temperatures are between 803 and 835°C, with an average of 819 ± 7°C. Perthitic exsolution in K-feldspar point to temperature lower than 600°C and P_{H2O} > 200 MPa (Bowen & Tuttle 1950) for the subsolidus stage.

Furthermore, a temperature of ~588°C obtained for the magnetite-ilmenite pair (Carmichael 1967) may reflect late- to post-magmatic reequilibration.

Oxygen fugacity (fO_2)

Redox conditions during magma crystallization can be qualitatively monitored by the fe# number [= Fe/(Fe+Mg)] of amphibole and biotite (e.g., Anderson & Smith 1995, Anderson *et al.* 2008). The analyzed amphibole and biotite crystals present fe# values between 0.90–0.92 and 0.89–0.9 respectively, which are indicative of relatively reducing crystallization conditions. Quantitative fO_2 estimation was done with the Amp-TB2 oxybarometer (Ridolfi 2021) and the improved Qtz-geobarometer of Yang *et al.* (2021) using, respectively, amphibole and whole rock compositions. The Amp-TB2 oxybarometer yielded oxygen fugacity values between –14.7 and –14.1, whereas higher values were obtained with the Qtz-geobarometer (–9.9 to –13.7). These f_{O2} values are slightly under the NNO (Ni-NiO) buffer ($-1.1 < \Delta_{NNO} < -0.5$) and confirm the relatively moderate to reducing crystallization environments for the SJCgr magmas. Such a conclusion is also supported by the scattering of samples through the reduced and slightly oxidized A-type granite fields in Fig. 8B.

It is worth mentioning that magnetite is a common accessory phase in some SCJgr varieties, and this may pose a contradiction with the above-inferred redox conditions. Although magnetite-bearing granites are generally interpreted as being "oxidized" (cf. Ishihara 1981), many authors have argued that, in fact, the presence of magnetite in granites is not incompatible with a more reduced character (cf. Dall'Agnol and Oliveira 2007, Campos *et al.* 2016).

U-Pb zircon geochronology

Sample ES471 (Latitude 6.236°S/Longitude 35.710°W; see location in Fig. 3 and whole composition in Suppl. Data Table 2) of the geochemically defined group 3 was selected for *in-situ* zircon U-Pb dating. The sample corresponds to a slightly deformed magnetite-apatite-amphibole-bearing medium- to coarse-grained granite (Figs. 4A and 4B) with euhedral zircon grains (length up to 0.9 mm), often with triangular terminations, crosscutting amphibole (Fig. 4B).

U-Pb analyses were performed on 37 zircon grains, totaling 44 spot analyses. The results are in Suppl. Data Table 3. Figures 11A and 11B display cathodoluminescence images of the analyzed grains. They usually have oscillatory zoning and prismatic habits and a bipyramidal shape, with an average length (L) of 243.5 ± 98.9 µm, width (W) of 92.6 ± 21.9 µm, and aspect ratios of L/W = 2.7 ± 1.1; Th/U ratio varies around 0.61 ± 0.17 (Th = 126 ± 145 ppm, U = 189 ± 158 ppm). Some zircon grains clearly present two growth generations with distinct age populations (Fig. 11B; spots z25c and z25r with $^{207}Pb/^{206}Pb$ ages of 2670 ± 24 Ma and 2613 ± 23 Ma, respectively). A group of 44 single analyses with < 5% of discordance yields intercepts at 2683 ± 22 and 724 ± 370 Ma (MSWD = 0.23; Fig. 11B). A total of 19 spots gave a concordia age of 2664 ± 13 Ma (MSWD = 2.8; inset in Fig. 11C). The age of 2664 ± 13 Ma is interpreted as the magmatic age. Slightly younger ages at 2605 ± 23 and 2582 ± 25 Ma (e.g., spots z26c and z26r in Fig. 11B) may represent a new generation of igneous zircon or post-magmatic lead loss. The results here obtained agree within the analytical errors with previous ages obtained by TIMS U-Pb zircon of 2683 ± 7 Ma (sample CE116B) and 2655 ± 4 Ma (sample EC80) by Dantas (1996).

DISCUSSION

Petrologic evolution

Differentiation mechanism and quantification of fractionation

Considering the curved trends in some Harker-type plots (e.g., CaO and MgO in Fig. 9), quantitative modeling of fractional crystallization was done for groups 2 (diorite to granite in Fig. 7A; SiO_2 = 58.49–67.8 wt. %) and 3 (granite to alkali-granite in Fig. 7A; 69.19–75.12 wt. %). Group 1 was not considered in modeling calculations, since it includes just one sample (ES407).

Compatible (Ni, Zr) vs. incompatible (Rb) trace element correlation (Fig. 12) suggests fractional crystallization mechanism as the main process of evolution for group 3 samples (cf. Cocherie 1986, Martin 1987). Accordingly, major element least-square mass-balance modeling was done with the spreadsheet PetroMode (Christiansen 2022). Mineral compositions are those reported herein (feldspars, amphiboles, biotite, magnetite, and ilmenite), besides apatite and pyroxenes from Deer *et al.* (2013). Further trace element modeling followed the classical fractional crystallization equation (Rayleigh 1896): $C_L = C_0F^{(D-1)}$, in which C_L = concentration of the trace element in the most evolved sample, C_0 = concentration of the trace element in the least evolved sample, F = (1-FC) [FC is the degree of fractional crystallization, with FC < 1], and D = bulk partition coefficient. The partition coefficients are those provided by the database from Nielsen (2022), as well as values reported for zircon by Martin (1987), Thomas *et al.* (2002), Rubatto and Hermann (2007), Burnham and Berry (2012), and Gudelius *et al.* (2020) and apatite by Prowatke and Klemme (2006). The precision of the modeling is monitored by the parameter Σr^2. The results for both groups 2 and 3 are shown in Table 1 and Figs. 13A and 13B.

For group 2, we considered L_0 = ES467 (SiO_2 = 59.7 wt. %, MgO = 4.3 wt. %, and Fe_2O_3t = 6.96 wt. %; anhydrous base) as the least differentiated sample, and L_1 = ES572 (SiO_2 = 66.19 wt. %, MgO = 1.39 wt. %, and Fe_2O_3t = 3.09 wt. %; anhydrous base) as the most differentiated one. The calculated liquid (C_{L2}') and cumulate (C_2) are in Table 1. Calculations indicate a FC degree of 40% with an excellent statistical error (Σr^2 = 0.31). The cumulate (C_2) has mainly plagioclase, hortonolite, and clinopyroxene that correspond to a gabbro-norite modal composition (Table 1). There is a very good adjustment for trace elements (compare C_{L2} and C_{L2}' in Table 1) that is also observed for the REE (Fig. 13A).

For group 3, we assumed L_0 = ES471 (SiO_2 = 69.89 wt. %, MgO = 0.31 wt. %, Fe_2O_3t = 5.38 wt. %; anhydrous base)

and CE116B (SiO_2 = 74.1 wt. %, MgO = 0.19 wt. %, Fe_2O_3t = 3.16 wt. %; anhydrous base) as the most differentiated sample (L_3). Modeling resulted in an excellent adjustment for major ($\Sigma r^2 = 0.02$), trace elements (Table 1; compare C_{L3} and C_{L3}' in Table 1), and REE (Fig. 13B). The cumulate C_3 contains mainly plagioclase, K-feldspar, magnetite, and hornblende, corresponding to a hornblende-magnetite-bearing monzonite modal composition (Table 1; compare with Figs. 4C and 4D). In cumulate C_3, traces of zircon were added to the model to adjust zirconium. It is worth mention the absence of biotite in both cumulates and the abundance of K-feldspar, hornblende, and magnetite in cumulate C_3.

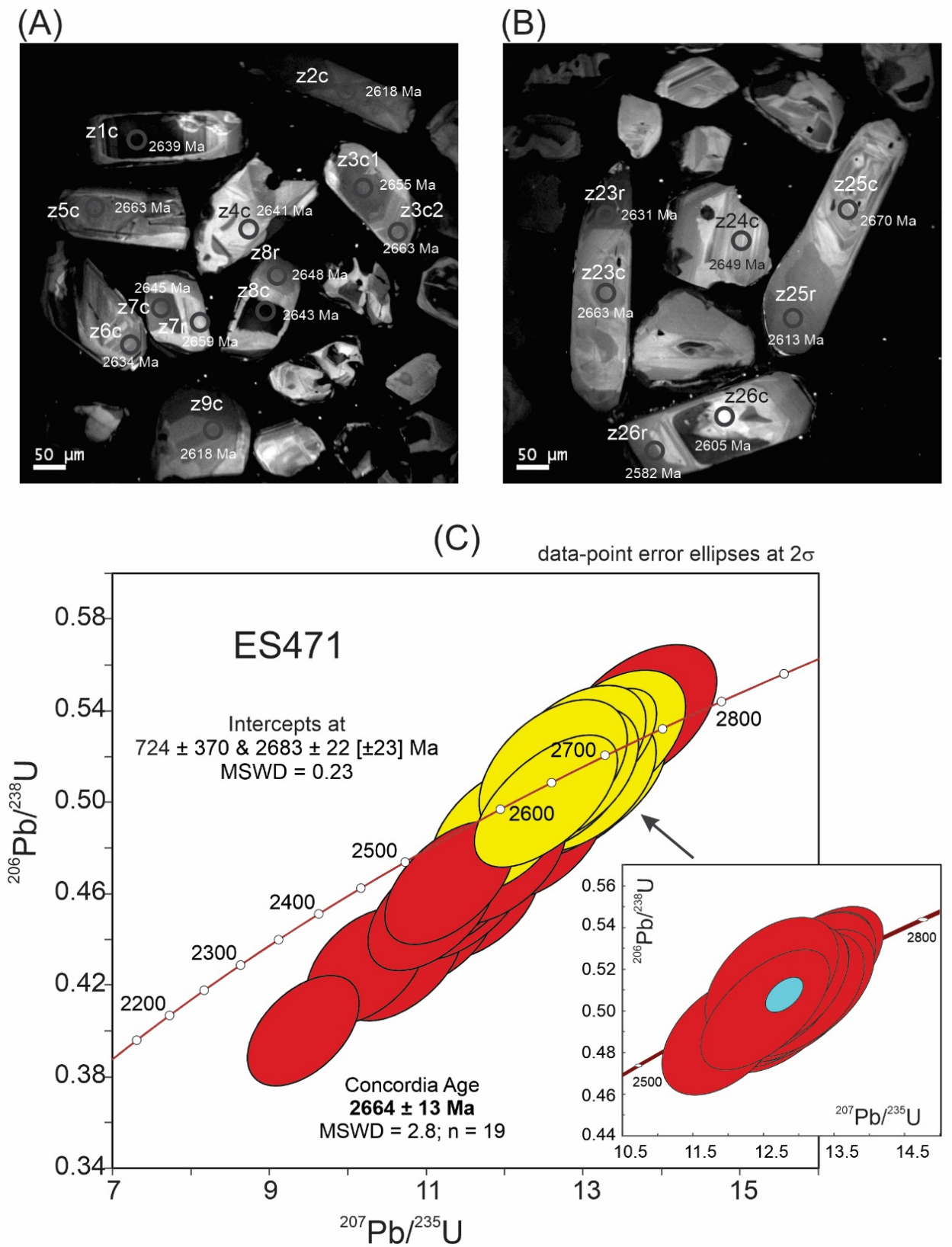

Figure 11. Zircon U-Pb results for sample ES471, southern portion of the São José do Campestre granite complex. (A and B) Zircon cathodoluminescence images. (C) Concordia diagram and weighted $^{206}Pb/^{238}U$ age of concordant zircons (concordance > 95%). Ages for displayed spots are $^{207}Pb/^{206}Pb$ date in million years (Suppl. Data Table 3).

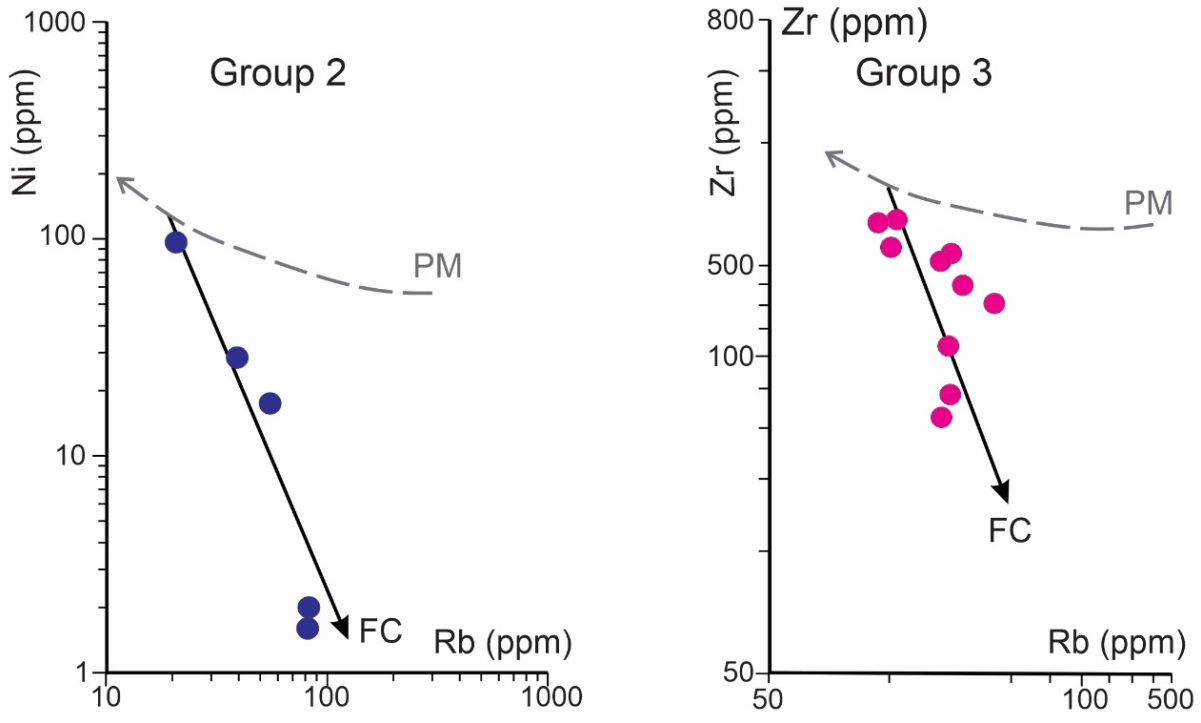

Figure 12. Incompatible (Rb) vs. compatible (Ni and Zr) trace element plots for groups (A) 2 and (B) 3.

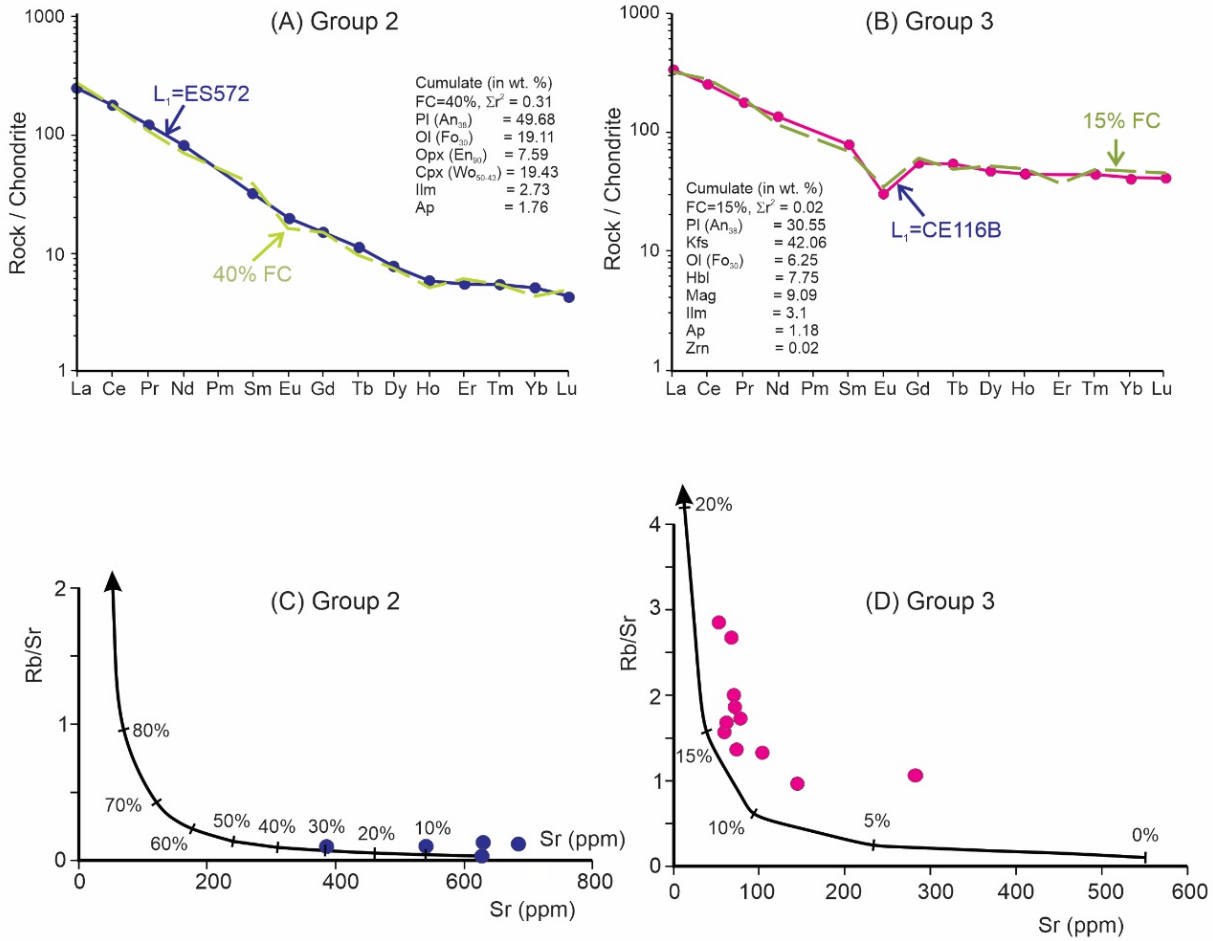

LCC: lower continental crust; FC: % of fractional crystallization.

Figure 13. Rare earth element spectra for quantitative modeling of (A and B) fractional crystallization and (C and D) crustal assimilation and fractional crystallization (AFC) modeling of the studied rocks in a Sr vs. Rb/Sr plot. (A) Group 2, with L_0 = sample ES467 and L_1 = sample ES572; (B) Group 3, with L_0 = sample ES471 and L_1 = sample CE116B (complete data in Suppl. Data Table 1). Cumulate compositions are in Table 1. Explanation for a and b: L_0 less evolved sample; L_1 more differentiated sample; C_2, C_3 cumulates for groups 2 and 3, respectively; Σr^2 statistical error. Abbreviations for minerals (Whitney and Evans 2010): Pl: plagioclase: Kfs: K-feldspar; Ol: olivine; Opx: orthopyroxene; Cpx: clinopyroxene; Ilm: ilmenite; Mag: magnetite; Ap: apatite; Zrn: zircon. In (C) and (D), the calculated AFC curves with a mass assimilation/fractionation ratio of 0.05 (= 5% crustal contamination) of the LCC (Wedepohl 1995) for groups 2 (ES467 evolves to ES572) and 3 (ES471 evolves to CE116B) are shown in (C) and (D), respectively. Mixing the calculation equation for trace elements after DePaolo (1981).

Crustal contamination

It has long been demonstrated that crustal assimilation coupled with fractional crystallization (AFC) is a relevant process during evolution of mantle-derived magmas through their ascent and emplacement into the lower and upper continental crust (DePaolo 1981, Huppert *et al.* 1985, Wilson 1989). For geochemical modeling, we have applied mixing equations of DePaolo (1981) and trace element composition of the lower continental crust (LCC; Wedepohl 1995). Calculations for different fractions of crustal material reveal the possibility of contamination of the dioritic (group 2) magma by ~5% of LCC, followed by 30–40% of fractional crystallization (Fig. 13C). Some amount of crustal contamination seems to account for group 3 set as well (Fig. 13D), which is corroborated by negative ε_{Nd}(2.7 Ga) of –4.02 to –6.18 (Suppl. Data Table 2).

Magma genesis and evolution

The geochemical characteristics described above suggest an upper mantle peridotite as the most probable source for the SCJgr complex. Any earlier crustal material would be impressed as a slab component (low- and high-silica adakites) hybridized with the upper mantle, leading to late Archean sanukitoids (or the ~2.6 to 2.5 Ga Closepet-type) and modern arc granitoids (Stern and Hanson 1991, Rapp *et al.* 1999, Smithies and Champion 2000, Moyen *et al.* 2001, 2003, Lobach-Zhuchenko *et al.* 2005, Martin *et al.* 2005, Nebel *et al.* 2018). This hybridized source should be LREE-enriched (e.g., Fig. 10). In this sense, the available ε_{Nd}(2.7 Ga) of –4.1 to –6.2 and Nd model age (T_{DM}) of 3.9–3.3 Ga for our samples (Dantas 1996, Dantas *et al.* 2013) support such an interpretation of an earlier crustal component that provided, by partial melting, the mixing component to the upper mantle peridotite (e.g., Jayananda *et al.* 2000, 2018, Nebel *et al.* 2018).

According to Wilson (1989), primary magmas derived directly from the upper mantle peridotite would have mg# > 70, Ni > 400–500 ppm, Cr > 1,000 ppm, and SiO_2 < 50 wt. %. The least evolved samples (ES407 of group 1 and ES467 of group 2) have SiO_2 = 53–58 wt. %, *mg#* = 53–58, Ni = 81–96 ppm, and Cr = 41–164 ppm and, therefore, may not represent primary melts. However, olivine (± chromite) fractionation at mantle depths from a primary basaltic melt would generate silica-enriched and Ni- and Cr-depleted liquids (Nicholls and Ringwood 1972) like the ones described here.

Moderate-to-low contents of Sc (25–15 ppm) in the least evolved sample (ES407, ES467) suggest the presence of minor garnet and amphibole in the source as these minerals have K_D^{Sc} >> 1 (Nielsen 2022). Through investigation of high-pressure experiments that produced saturated tholeiites, andesitic, and dacitic melts, Nicholls and Ringwood (1972) and Green (1973) suggested that they were generated by partial melting of hydrous mantle peridotite (with pargasitic amphibole) followed by different degrees of fractional crystallization of olivine at mantle or crustal depths. Moreover, petrological constraints from high-pressure experimental runs discussed by Pilet (2015) led to assume a lithosphere metasomatized by amphibole-bearing veins as the most probable source of sodic (Na_2O/K_2O > 1), mantle-derived magmas. This agrees with the less evolved samples having Na_2O/K_2O = 3.3–2.0 wt. %.

Figure 14 summarizes the polybaric evolution of the studied rocks. The first stage is the partial melting of a hydrous metasomatized mantle peridotite (probably with garnet and/or spinel, pargasitic amphibole, and phlogopite), forming a basaltic to andesitic magma at pressures of 2.5–3.0 GPa (~85 to 102 km) and temperatures of 1,000–1,200°C. In the second stage, these magmas underwent olivine fractionation at mantle and/or crustal depths giving origin to our less evolved samples (ES407 and ES467). The third stage comprises fractional crystallization (± crustal assimilation) under pressures of ~400 to 600 MPa (~15 to 23 km) and temperatures > 800°C, under reducing to slightly oxidizing conditions that has left olivine gabbro-norite or olivine monzonite cumulates (Table 1).

Tectonic setting and geodynamic implication

Figure 15 shows the investigated samples in ocean ridge granite (ORG)-normalized multi-element diagram. Group 1 sample ES407 (Fig. 15A) displays a spectrum with an inclination (Rb_N/Y_N) of 29.4, Yb_N = 0.02, and Y_N = 0.28, and no significant anomalies. These signatures share similarities with basaltic andesites of the Andean Central Volcanic Zone (Thorpe *et al.* 1984).

Figures 15B and 15C present four representative samples of group 2 and three of group 3. Both sets have steeper patterns and similar Rb_N/Y_N ratios (averages of 35.4 ± 29.2 and 35.9 ± 12.6, respectively). Group 2 may display positive anomalies for Ba (3.3 ± 2.9) and Ce (7.2 ± 5.3). These anomalies are slightly lower in group 3. Group 2 patterns can be compared to those found in the Andean Costal Batholiths (Petford and Atherton 1996) and Volcanic Arc Granites (Pearce *et al.* 1984), whereas group 3 has slightly higher normalized contents of Ce to Yb.

Whole rock compositions of the studied SJCgr samples indicate that these rocks correspond to slightly oxidizing to reduced A_2-type granites (Figs. 7A–7C) with some degree of crustal contamination that is reflected in their normative corundum <0.5 wt. %, and A/NK and A/CNK ratios of > 1.1 and < 1, respectively. Their trace element contents are akin to post-collisional granites, with some samples showing geochemical characteristics of volcanic arc granites (Fig. 7D). This agrees with the preservation of igneous features and rock relationships (Fig. 3), as well as microscopic textures (Fig. 4). Furthermore, the REE patterns point to a subduction tectonic setting for their genesis and evolution. In this tectonic environment, the subducting oceanic crust and the overlying mantle wedge are the main magma reservoirs. We explored this hypothesis in a SiO_2 vs. *mg#* binary diagram by plotting both our samples and experimental results from the literature (Fig. 16). Group 1 (sample ES407; SiO_2 53.9 wt. %, *mg#* 54.2) is the closest to the field of mantle-derived melts. The less evolved group 2 sample ES467 (SiO_2 58.5 wt. %, *mg#* 55) lies in between low-silica adakites and high-silica adakites and almost overlaps the average of sanukitoids (SiO_2 58.8 wt. %, *mg#* 56.8). Group 2 samples ES543A and ES572 have SiO_2 and *mg#* of ~65 wt. % and 46, respectively and plot between high-silica adakites and modern arc granitoids (SiO_2 ~65 to 68 wt. %, *mg#* ~48 to 81). Group 1 sample ES407 and the least evolved sample from group 2 (ES467)

scatter among the field of hybridized melts (slab-derived melts mixed in different proportions with mantle-derived melts; Rapp *et al.* 1999). The remaining samples have SiO_2 > 67 wt. % and *mg#* < 20, falling out of the field of slab melts. This means that this kind of source cannot explain the compositional variation of the studied rocks. Hence, they may be explained as late differentiates from basic to intermediate parental liquids, as highlighted in Fig. 16.

The timing of the magma generation and the subduction/collisional process are difficult to assess (Condie 1989, Davidson and Arculus 2006). Nevertheless, delamination of the continental lithospheric mantle (Rudnick 1995), underplating of basaltic magma at the base of the lower continental crust (Huppert *et al.* 1988), and even the action of mantle plumes (Abbott 1996, Condie 2001) could not be discarded.

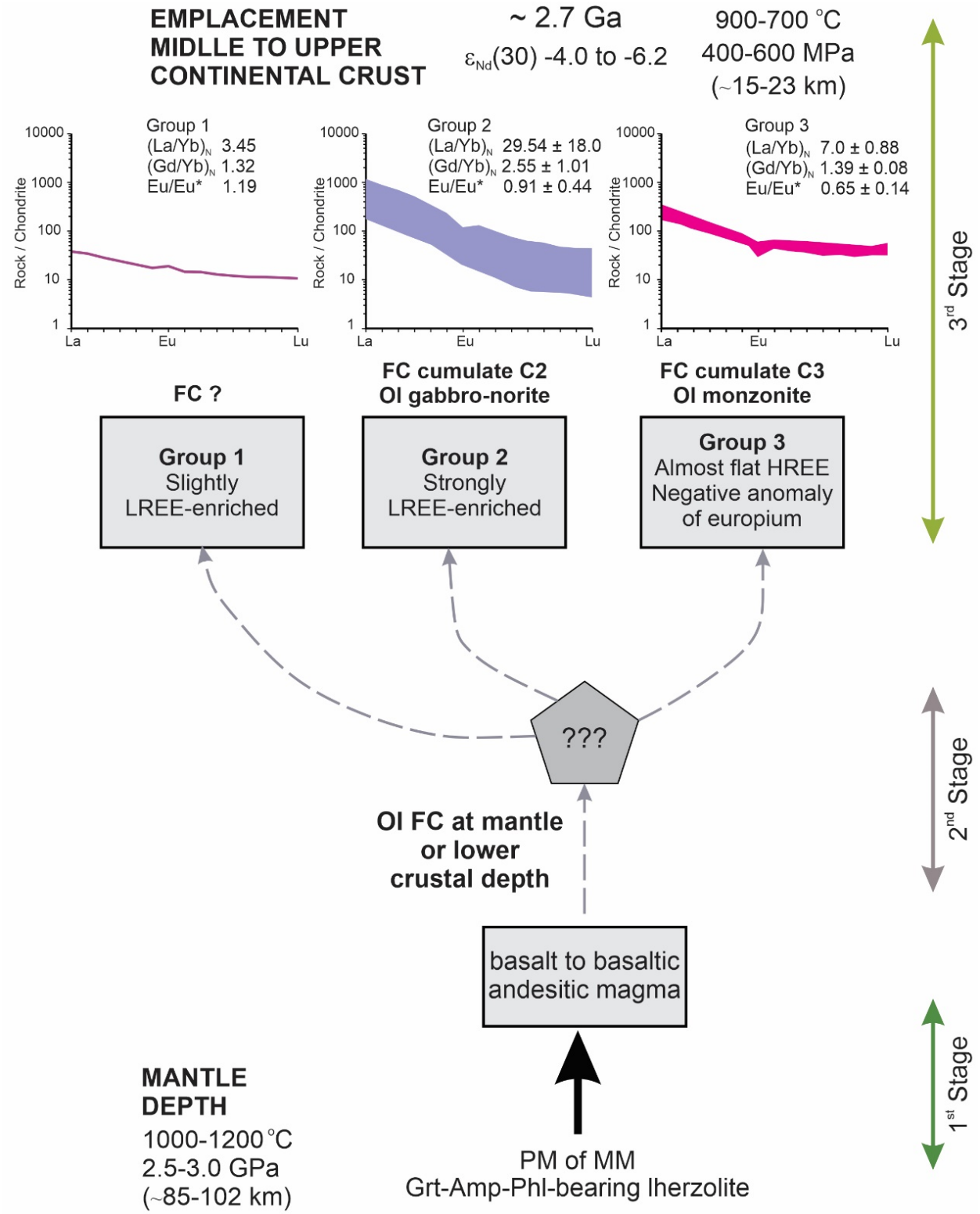

PM: partial melting; FC: fractional crystallization; MM: metasomatized mantle; Ol: olivine; Grt: garnet; Amp: amphibole: Phl: phlogopite; LREE: light rare earth elements; HREE: heavy rare earth elements; Cum: cumulate; C2: olivine gabbro-norite; C3: olivine monzonite.

Figure 14. Schematic evolution stages for the studied rocks (see Table 1 and Figs. 13A and 13B).

Nebel *et al.* (2018) consider that heat from ascending hot, high-Mg sanukitoid magmas, formed earlier through interaction of TTG melts with the asthenospheric mantle, triggers melting of lower crust material to generate late Archean high-K granites, the entire evolution extending for > 200 Ma. Based on the Nd model age (T_{DM}) of clinopyroxene from peridotite xenoliths in alkaline and kimberlitic magmas, Menzies *et al.* (1987) stated that the metasomatism of upper mantle peridotite by silicate melts and hydrous fluids is a very early event. According to Menzies *et al.* (1987), this event could take place ~0.5 to 1 Ga before the crystallization age, and even much older than 1 Ga beneath cratons. This time lapse estimation lies within the SJCgr intrusion age interval of ~2.7 Ga (Fig. 12C) and within the Nd model ages of 3.9–3.3 Ga (Dantas 1996, Dantas *et al.* 2013).

Several episodes of juvenile accretion and crustal recycling have been suggested based on zircon U-Pb data for the São José do Campestre Massif (SJCM) by Dantas *et al.* (2013) and Souza *et al.* (2016): 3.5–3.4 Ga, 3.36 Ga, 3.25 Ga, 3.18 Ga, 3.12 Ga, 3.03 Ga, and 2.69 Ga. In an exhaustive compilation of zircon U-Pb and Nd model ages, Ganade *et al.* (2021) stated that the SJCM is one smaller cratonic blocks in northeastern Brazil that resulted from fragmentation of the São Francisco — Congo — West Africa cratons followed by successive collisions during the Proterozoic. In this regard, somewhat analogous events of crust formation are depicted for the Mairi complex, northern São Francisco Craton, by Oliveira *et al.* (2020) and Moreira *et al.* (2022), where banded gneisses (TTG-like felsic layers alternating with metamorphosed gabbro-diorite bands) have zircon U-Pb ages of 3.7–3.6 Ga. For the same complex, Moreira *et al.* (2022) described successive younger events of crustal growth at 3.55–3.52, 3.49–3.33, and 2.74–2.58 Ga, with main crustal recycling events in the Neoarchean. Similar magmatic events and post-collisional granite emplacement are also documented in southeastern Brazil (Marimon *et al.* 2022) and in the Dharwar craton (e.g., Jayananda *et al.* 2006, Sebastian *et al.* 2021, Kumar *et al.* 2022). In the latter case, however, they assumed that the last Neoarchean episode was marked by juvenile, mantle-derived magmatism with some degree of crustal component. This could be accommodated by convergent tectonic settings (island arcs or continental margin-types) and the widespread amalgamation of earlier Archean units. Therefore, the data here obtained for the SJCgr complex show that global plate tectonics was the main process involved in the generation of continental crust in the SJCM, as also proposed for the Southern Brasília Orogen and the Southern São Francisco Craton (Marimon *et al.* 2022).

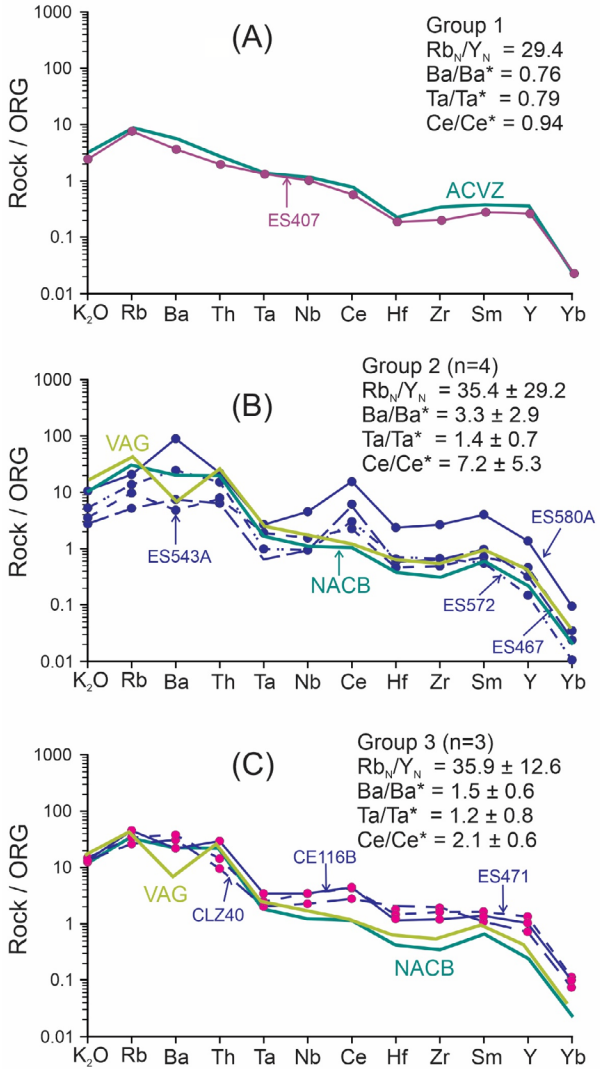

Ba/Ba*: anomaly of Ba [$Ba_N/((Rb_N + Th_N)/2)$]; Ta/Ta*: anomaly of Ta [$Ta_N/((Th_N + Nb_N)/2$]; Ce/Ce*: anomaly of Ce [$Ce_N/((Nb_N + Hf_N)/2$].

Figure 15. Ocean-ridge-granite (ORG; Pearce *et al.* 1984) normalized multielement plot for the studied rocks. (A) Group 1 compared to basaltic andesite from the Andean Central Volcanic Zone (ACVZ; Thorpe *et al.* 1984). (B and C) Groups 2 and 3, respectively, compared to granodiorite from the Northern Andean Coastal Batholith (NACB; Petford and Atherton 1996) and volcanic arc granite (VAG; Pearce *et al.* 1984).

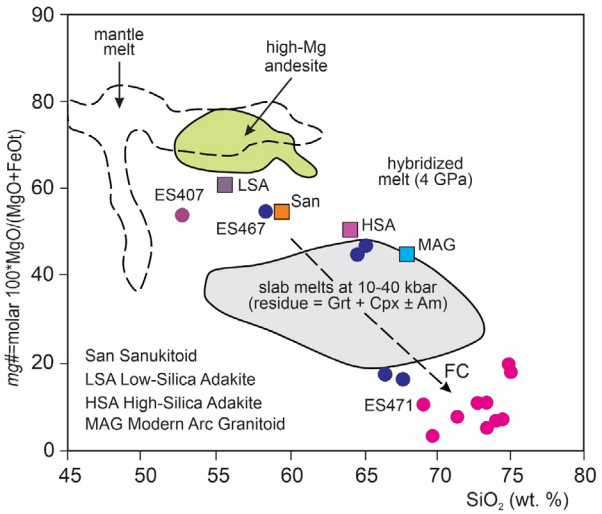

Figure 16. SiO_2 vs. *mg#* for the studied rocks and experimental results from the literature. References: Mg-andesites, slab melt and hybridized melt from Rapp *et al.* (1999 and references therein); low-silica and high-silica adakites from Martin *et al.* (2005); sanukitoid from Martin *et al.* (2005, 2009); modern arc granitoids from Martin *et al.* (2009); mantle melts from Baker and Stolper (1994), Hirose (1997), Hirschmann *et al.* (1998), Robinson *et al.* (1998), Wasylenki *et al.* (2003), Condamine and Médard (2014), and Condamine *et al.* (2016). Abbreviations for minerals (according to Whitney and Evans 2010): Grt: Garnet; Am: amphibole; Cpx: clinopyroxene.

CONCLUSION

Integration of the data reported here and those in the existing literature led to the main conclusions listed below.

- Field relations, petrographic, textural, and geochemical data, and in-situ U-Pb dating reveal that the plutonic rocks forming the São José do Campestre granite complex, northeastern Brazil, vary from gabbro to granite with preserved igneous textures and fabrics (e.g., Dantas *et al*. 2013, Souza *et al*. 2016).
- Laser ablation zircon U-Pb dating indicates a Concordia age of 2664 ± 13 Ma, which is considered the emplacement age (e.g., Dantas *et al*. 2004).
- The rocks are metaluminous, calc-alkaline to transitional to alkaline, LILE-, and LREE-enriched, with chemical signatures akin to slightly oxidized to reduced post-collisional A_2-type granites.
- Based on geochemical data, three rock groups are defined: Group 1, one sample, SiO_2 = 59.7 wt. %, MgO = 5.46 wt. %; Group 2, five samples, SiO_2 = 59.7–68.23 wt. %, MgO = 4.3–0.6 wt. %; Group 3, ten samples, SiO_2 = 69.9–75.1 wt. %, MgO = 0.1–0.3 wt. %.
- The petrogenetic evolution of the SCJgr occurred as follows: 1st — partial melting of a metasomatized (with minor amounts of spinel ± garnet, amphibole, phlogopite) upper mantle peridotite (~83–100 km, 1,000–1,200°C), generating a basaltic to basaltic andesitic magma; 2nd — fractional crystallization of olivine at mantle or subcrustal depths, leading to the less evolved samples of each group; 3rd — 40–15% fractional crystallization giving rise to the magmatic series and olivine gabbro-norite and olivine monzonite cumulates (15–23 km, > 800°C).
- This magmatism has major and trace element contents analogous to late Archean sanukitoid and modern arc granitoids.
- The SJCgr complex represents the last Neoarchean episode of mantle-derived magma (and is related to some kind of plate tectonics) and marks the amalgamation of all earlier Archean blocks of the studied cratonic block.

ACKNOWLEDGMENTS

This article is a tribute to Professor Hervé Martin, who sadly passed away 1 year ago. ZSS is particularly indebted to Professor Hervé as his supervisor of the DESS (Diplôme d´Études en Sciences, Université de Rennes, 1991) and a post-doctoral sabbatical stage (Université Blaise Pascal, Clermont-Ferrand, 1997). In both situations, the focus was on the acquisition and interpretation of whole rock chemistry and isotopic data from Archean to Early Proterozoic juvenile granitoids of NE Brazil. Professor Hervé always made complex topics simpler with joy, good humor, and fine intelligence. He was really a great scholar and scientist. Thank you very much for all the learning you gave us. The authors acknowledge the Programa de Pos-Graduação em Geodinâmica e Geofísica and the Departamento de Geologia of the Universidade Federal do Rio Grande do Norte (PPGG/UFRN and DGeo/UFRN) for supporting field and laboratory works. The Conselho Nacional de Desenvolvimento Científico e Tecnológico (CNPq) is acknowledged for financial support (grant number 408607/2018-1). The authors also thank Nilson Francisquini Botelho (Instituto de Geociências, Universidade de Brasília) for helping with mineral chemical data acquisition and fruitful discussions and Alexandre H. Santos Filho for microscopic image acquisition.

ARTICLE INFORMATION

Manuscript ID: 20220079. Received on: 11 OCT 2022. Approved on: 15 MAR 2023.

How to cite this article: Souza Z.S., Dantas E.L., Oliveira E.P., Vilalva F.C.J., Motta R.G., Martin H., Valcáio S.N. 2023. Zircon U-Pb dating and petrogenesis of the São José do Campestre Granite Complex, NE Brazil: an example of neoarchean mantle-derived post-collisional magmatism. *Brazilian Journal of Geology*, **53**(2):e20220079. https://doi.org/10.1590/2317-4889202320220079

Z.S.S.: Conceptualization, Data curation, Funding acquisition, Investigation, Methodology, Project administration, Resources, Supervision, Validation, Visualization, Writing—original draft, Writing—review & editing. E.L.D.: Investigation, Methodology, Writing—original draft. E.P.O.: Methodology, Validation, Writing—original draft, Writing—review & editing. F.C.J.V.: Investigation, Methodology, Supervision, Validation, Writing—original draft, Writing—review & editing. R.G.M.: Investigation, Methodology, Writing—original draft. H.M.: Conceptualization. S.N.V.: Investigation, Methodology, Visualization.

Competing interest: the authors declare that there are no competing interests.

REFERENCES

Abbott D.H. 1996. Plumes and hot spots as sources of greenstone belts. *Lithos*, **37**(2-3):113-127. https://doi.org/10.1016/0024-4937(95)00032-1

Abbott D.H., Burgess L., Longhi J., Smith W.H.F. 1994. An empirical thermal history of the upper mantle. *Journal of Geophysical Research*, **99**(B7):13835-13850. https://doi.org/10.1029/94JB00112

Almeida F.F.M., Hasui Y., Brito Neves B.B., Fuck R. 1981. Brazilian structural provinces: an introduction. *Earth Science Reviews*, **17**(1-2):1-29. https://doi.org/10.1016/0012-8252(81)90003-9

Anderson J.L., Barth A.P., Wooden J.L., Mazdab F. 2008. Thermometers and thermobarometers in granitic systems. *Reviews in Mineralogy and Geochemistry*, **69**(1):121-142. https://doi.org/10.2138/rmg.2008.69.4

Anderson J.L., Smith D.R. 1995. The effects of temperature and f_{O2} on the Al-in-hornblende barometer. *American Mineralogist*, **80**(5-6):549-559. https://doi.org/10.2138/am-1995-5-614

Angelim L.A.A., Vasconcelos A.M., Gomes J.R.C., Wanderley A.A., Forgiarini L.L., Medeiros M.F. 2004. *Folha SB.24-Jaguaribe*. In: Schobbenhaus C., Gonçalves J.H., Santos J.O.S., Abram M.B., Leão Neto R., Matos G.M.M., Vidotti R.M., Ramos M.A.B., Jesus J.D.A. (eds.). *Carta Geológica do Brasil ao Milionésimo*. Programa Geologia do Brasil. Brasília: CPRM. Available at: https://rigeo.cprm.gov.br/handle/doc/4978. Accessed on: Aug. 4, 2022.

Arthaud M.H., Caby R., Fuck R.A., Dantas E.L., Parente C.V. 2008. Geology of the northern Borborema Province, NE Brazil and its correlation with Nigeria, NW Africa. In: Pankhurst R.J., Trouw R.A.J., Brito Neves B.B., De Wit M.J. (Eds.). *West Gondwana*. Pre-Cenozoic correlations across the South Atlantic region. Geological Society of London, Special Publication, **294**(1):49-76. https://doi.org/10.1144/SP294.4

Baker M.B., Stolper E.M. 1994. Determining the composition of high-pressure mantle melts using diamond aggregates. *Geochimica et Cosmochimica Acta*, **58**(13):2811-2827. https://doi.org/10.1016/0016-7037(94)90116-3

Barker F., Arth J.G. 1976. Generation of trondhjemitic-tonalitic liquids and Archaean bimodal trondhjemite-basalt suites. *Geology*, **4**(10):596-600. https://doi.org/10.1130/0091-7613(1976)4<596:GOTLAA>2.0.CO;2

Blundy J., Cashman K. 2001. Ascent-driven crystallisation of dacite magmas at Mount St Helens, 1980–1986. *Contributions to Mineralogy and Petrology*, **140**:631-650. https://doi.org/10.1007/s004100000219

Bowen N.L., Tuttle O.F. 1950. The System $NaAlSi_3O_8$-$KAlSi_3O_8$-H_2O. *Journal of Geology*, **58**(5):489-511. https://doi.org/10.1086/625758

Burnham A.D., Berry A.J. 2012. An experimental study of trace element partitioning between zircon and melt as a function of oxygen fugacity. *Geochimica et Cosmochimica Acta*, **95**:196-212. https://doi.org/10.1016/j.gca.2012.07.034

Caby R., Sial A.N., Arthaud M. Vauchez A. 1991. Crustal Evolution and the Brasiliano Orogeny in Northeast Brazil. In: Dallmeyer R.D., Lécorché J.P. (Eds.). *The West African Orogens and Circum-Atlantic Correlatives*. IGCP-Project 233. Berlin, Heidelberg: Springer, p. 373-397. https://doi.org/10.1007/978-3-642-84153-8_16

Campos B.C.S., Vilalva F.C.J., Nascimento M.A.L., Galindo A.C. 2016. Crystallization conditions of porphyritic high-K calc-alkaline granitoids in the extreme northeastern Borborema Province, NE Brazil, and geodynamic implications. *Journal of South American Earth Sciences*, **70**:224-236. https://doi.org/10.1016/j.jsames.2016.05.010

Carmichael I.S.E. 1967. The iron-titanium oxides of salic volcanic rocks and their associated ferromagnesian silicates. *Contributions to Mineralogy and Petrology*, **14**:36-64. https://doi.org/10.1007/BF00370985

Castillo P.R. 2006. An overview of adakite petrogenesis. *Chinese Science Bulletin*, **51**:257-268. https://doi.org/10.1007/s11434-006-0257-7

Castillo P.R. 2012. Adakite petrogenesis. *Lithos*, **134-135**:304-316. https://doi.org/10.1016/j.lithos.2011.09.013

Caxito F.A., Santos L.C.M.L., Ganade C.E., Bendaoud A., Fettous E.-H., Bouyo M.H. 2020. Toward an integrated model of geological evolution for NE Brazil-NW Africa: the Borborema province and its connections to the Trans-Saharan (Benino-Nigerian and Tuareg shields) and Central African orogens. *Brazilian Journal of Geology*, **50**(2):e20190122. https://doi.org/10.1590/2317-4889202020190122

Christiansen E.H. 2022. *PetroMode*. Brigham Young University. Available at: http://hdl.lib.byu.edu/1877/2708. Accessed on: July 23, 2022.

Cocherie A. 1986. Systematic use of trace element distribution patterns in log-log diagrams for plutonic suites. *Geochimica et Cosmochimica Acta*, **50**(11):2517-2522. https://doi.org/10.1016/0016-7037(86)90034-7

Condamine P., Médard E. 2014. Experimental melting of phlogopite-bearing mantle at 1 GPa: Implications for potassic magmatism. *Earth and Planetary Science Letters*, **397**:80-92. https://doi.org/10.1016/j.epsl.2014.04.027

Condamine P. Médard E., Devidal J.L. 2016. Experimental melting of phlogopite-peridotite in the garnet stability field. *Contributions to Mineralogy and Petrology*, **171**:95. https://doi.org/10.1007/s00410-016-1306-0

Condie K.C. 1976. Trace-element Geochemistry of Archean Greenstone Belts. *Earth-Science Reviews*, **12**(4):393-417. https://doi.org/10.1016/0012-8252(76)90012-X

Condie K.C. 1981. *Archean Greenstone Belts*. Amsterdam: Elsevier, 434 p.

Condie K.C. 1989. *Plate Tectonics and Crustal Evolution*. Oxford: Pergamon Press, 476 p.

Condie K.C. 2001. *Mantle Plumes and their Record in Earth History*. Cambridge: Cambridge University Press, 306 p.

Cox K.G., Bell J.D., Pankhurst R.J. 1979. *The interpretation of the igneous rocks*. London: Allen and Unwin, 450 p.

Dall'Agnol R., Oliveira D.C. 2007. Oxidized, magnetite-series, rapakivi-type granites of Carajás, Brazil: Implications for classification and petrogenesis of A-type granites. *Lithos*, **93**(3-4):215-233. https://doi.org/10.1016/j.lithos.2006.03.065

Dantas E.L. 1996. *Geocronologia U-Pb e Sm-Nd de terrenos arqueanos e paleoproterozóicos do Maciço Caldas Brandão, NE do Brazil*. PhD Thesis, UNESP, Rio Claro, Brazil, 206 p.

Dantas E.L., Souza Z.S., Wernick E., Hackspacher P.C., Xiaodong D. Li J.W. 2013. Crustal growth in the 3.4-2.7 Ga São José de Campestre Massif, Borborema Province, NE Brazil. *Precambrian Research*, **227**:120-156. https://doi.org/10.1016/j.precamres.2012.08.006

Dantas E.L., Van Schmus W.R., Hackspacher P.C., Fetter A.H., Brito Neves B.B., Cordani U.G., Nutman A.P. Williams I.S. 2004. The 3.4-3.5 Ga São José do Campestre massif, NE Brazil: remnants of the oldest crust in South America. *Precambrian Research*, **130**(1-4):113-137. https://doi.org/10.1016/j.precamres.2003.11.002

Davidson J.P., Arculus R.J. 2006. The significance of Phanerozoic arc magmatism in generating continental crust. In: Brown M. & Rushmer T. (Eds.). *Evolution and Differentiation of the Continental Crust*. Cambridge: Cambridge University Press, p. 134-172.

Deer W.A., Howie R.A., Zussman J. 2013. *An introduction to the rock-forming minerals*. London: Mineralogical Society, 498 p.

Defant M.J., Drummond M.S. 1990. Derivation of some modern arc by melting of young subducted lithosphere. *Nature*, **347**:662-665. https://doi.org/10.1038/347662a0

DePaolo D.J. 1981. Trace element and isotopic effects of combined wall rock assimilation and fractional crystallization. *Earth and Planetary Science Letters*, **53**(2):189-202. https://doi.org/10.1016/0012-821X(81)90153-9

Drummond M.S., Defant M.J. 1990. A model for trondhjemite-tonalite-dacite genesis and crustal growth via slab melting: Archean to modern comparisons. *Journal of Geophysical Research*, **95**(B13):21503-21521. https://doi.org/10.1029/JB095iB13p21503

Ferreira A.C.D., Dantas E.L., Fuck R.A., Nedel I.M. 2020. Arc accretion and crustal reworking from late Archean to Neoproterozoic in Northeast Brazil. *Scientific Reports*, **10**:7855. https://doi.org/10.1038/s41598-020-64688-9

Ferreira A.C.D., Dantas E.L., Fuck R.A., Nedel I.M., Reimold W.U. 2021. Multiple stages of migmatite generation during the Archean to Proterozoic crustal evolution in the Borborema Province, Northeast Brazil. *Gondwana Research*, **90**:314-334. https://doi.org/10.1016/j.gr.2020.09.005

Frost B.R., Barnes C.G., Collins W.J., Arculus R.J., Ellis D.J., Frost C.D. 2001. A chemical classification for granitic rocks. *Journal of Petrology*, **42**(11):2033-2048. https://doi.org/10.1093/petrology/42.11.2033

Ganade C.E., Weinberg R.F., Caxito F.A., Lopes L.B.L., Tesser L.R., Costa I.S. 2021. Decratonization by rifting enables orogenic reworking and transcurrent dispersal of old terranes in NE Brazil. *Scientific Reports*, **11**:5719. https://doi.org/10.1038/s41598-021-84703-x

Grebennikov A.V. 2014. *A*-type granites and related rocks: petrogenesis and classification. *Russian Geology and Geophysics*, **55**(9):1074-1086. https://doi.org/10.1016/j.rgg.2014.08.003

Green D.H. 1973. Experimental melting studies on a model upper mantle composition at high pressure under water-saturated and water-undersaturated conditions. *Earth and Planetary Science Letters*, **19**(1):37-53. https://doi.org/10.1016/0012-821X(73)90176-3

Gudelius D., Zeh A., Almeev R.R., Wilson A.H., Fischer L.A., Schmitt A.K. 2020. Zircon melt inclusions in mafic and felsic rocks of the Bushveld Complex - Constraints for zircon crystallization temperatures and partition coefficients. *Geochimica et Cosmochimica Acta*, **289**:158-181. https://doi.org/10.1016/j.gca.2020.08.027

Guo B., Liu S., Chen X., Wang W., Guo R., Yan M. 2018. K-rich granitoid magmatism at the Archean–Proterozoic transition in southern Jilin: Insights into the Neoarchean crustal evolution of the northeastern part of the North China Craton. *Gondwana Research*, **58**:87-104. https://doi.org/10.1016/j.gr.2018.02.013

Harrison T.M., Watson E.B. 1984. The behavior of apatite during crustal anatexis: equilibrium and kinetic considerations. *Geochimica et Cosmochimica Acta*, **48**(7):1467-1477. https://doi.org/10.1016/0016-7037(84)90403-4

Hawthorne F.C., Oberti R., Harlow G.E., Maresch W.V., Martin R.F., Schumacher J.C., Welch M.D. 2012. Nomenclature of the amphibole supergroup. *American Mineralogist*, **97**(11-12):2031-2048. https://doi.org/10.2138/am.2012.4276

Heilimo E., Halla J., Holtta P. 2010. Discrimination and origin of the sanukitoid series: geochemical constraints from the Neoarchean western Karelian Province (Finland). *Lithos*, **115**(1-4):27-39. https://doi.org/10.1016/j.lithos.2009.11.001

Herzberg C. 2016. Petrological evidence from Komatiites for an early Earth carbon and water cycle. *Journal of Petrology*, **57**(11-12):2271-2288. https://doi.org/10.1093/petrology/egw055

Hirose K. 1997. Melting experiments on lherzolite KLB-1 under hydrous conditions and generation of high-magnesian andesitic melts. *Geology*, **25**(1):42-44. https://doi.org/10.1130/0091-7613(1997)025<0042:MEOLKU>2.3.CO;2

Hirschmann M.M., Baker M.B., Stolper E.M. 1998. The effect of alkalis on the silica content of mantle-derived melts. *Geochimica et Cosmochimica Acta*, **62**(5):883-902. https://doi.org/10.1016/S0016-7037(98)00028-3

Hollanda M.H.B.M., Archanjo C.J., Souza L.C., Liu D., Armstrong R. 2011. Long-lived Paleoproterozoic granitic magmatism in the Seridó-Jaguaribe domain, Borborema Province - NE Brazil. *Journal of South American Earth Sciences*, **32**(4):287-300. https://doi.org/10.1016/j.jsames.2011.02.008

Huppert H.E., Stephen R., Sparks R.S.J. 1985. Cooling and contamination of mafic and ultramafic magmas during ascent through the continental crust. *Earth and Planetary Science Letters*, **74**(4):371-386. https://doi.org/10.1016/S0012-821X(85)80009-1

Huppert H.E., Stephen R., Sparks R.S.J. 1988. The Generation of Granitic Magmas by Intrusion of Basalt into Continental Crust. *Journal of Petrology*, **29**(3):599-624. http://dx.doi.org/10.1093/petrology/29.3.599

Ishihara S. 1981. The granitoid series and mineralization. *Economic Geology*, **75**:458-484. https://doi.org/10.5382/AV75.14

Jahn B.M., Glikson A.Y., Peucat J.J., Hickamn A.H. 1981. REE geochemistry and isotopic data of Archaean silicic volcanics and granitoids from the Pilbara Block, western Australia: implications for the early crustal evolution. *Geochimica et Cosmochimica Acta*, **45**(9):1633-1652. https://doi.org/10.1016/S0016-7037(81)80002-6

Jayananda M., Chardon D., Peucat J.-J., Capdevila R. 2006. 2.61 Ga potassic granites and crustal reworking in the western Dharwar craton, southern India: Tectonic, geochronologic and geochemical constraints. *Precambrian Research*, **150**(1-2):1-26. https://doi.org/10.1016/j.precamres.2006.05.004

Jayananda M., Martin H., Peucat J.J., Mahabaleswar B. 1995. Late Archaean crust-mantle interactions: geochemistry of LREE-enriched mantle derived magmas. Example of the Closepet batholith, southern India. *Contributions to Mineralogy and Petrology*, **119**:314-329. https://doi.org/10.1007/BF00307290

Jayananda M., Moyen J.-F., Martin H., Peucat J.-J., Auvray B., Mahabaleswar B. 2000. Late Archaean (2550–2520 Ma) juvenile magmatism in the Eastern Dharwar craton, southern India: constraints from geochronology, Nd–Sr isotopes and whole rock geochemistry. *Precambrian Research*, **99**(3-4):225-254. https://doi.org/10.1016/S0301-9268(99)00063-7

Jayananda M., Santosh M., Aadhiseshan K.R. 2018. Formation of Archean (3600-2500 Ma) continental crust in the Dharwar Craton, southern India. *Earth-Science Reviews*, **181**:12-42. https://doi.org/10.1016/j.earscirev.2018.03.013

Kumar B.T., Jayananda M., Nasipuri P., Guitreau M., Aadhiseshan K.R., Balaji S.V., Rao M., Thomas T.T., Satyanarayanan M. 2022. Tectono-thermal history of the Neoarchean Balehonnur Shear Zone, Western Dharwar Craton (Southern India). GeoScienceWorld *Lithosphere*, **2022**(Spe. 8):4167477. https://doi.org/10.2113/2022/4167477

Lameyre J., Bowden P. 1982. Plutonic rock type series: discrimination of various granitoid series and related rocks. *Journal of Volcanology and Geothermal Research*, **14**(1-2):169-186. https://doi.org/10.1016/0377-0273(82)90047-6

Laurent O., Björnsen J., Wotzlaw J.F., Bretscher S., Pimenta Silva M., Moyen J.F., Ulmer P., Bachmann O. 2020. Earth's earliest granitoids are crystal-rich magma reservoirs tapped by silicic eruptions. *Nature Geoscience*, **13**:163-169. https://doi.org/10.1038/s41561-019-0520-6

Laurent O., Martin H., Moyen J.F., Doucelance R. 2014. The diversity and evolution of late-Archean granitoids: Evidence for the onset of "modern-style" plate tectonics between 3.0 and 2.5 Ga. *Lithos*, **205**:208-235. https://doi.org/10.1016/j.lithos.2014.06.012

Lobach-Zhuchenko S.B., Rollinson H.R., Chekulaev V.P., Arestova N.A., Kovalenko A.V., Ivanikov V.V., Guseva N.S., Sergeev S.A., Matukov D.I., Jarvis K.E. 2005. The Archaean sanukitoid series of the Baltic Shield: geological setting, geochemical characteristics and implications for their origin. *Lithos*, **79**(1-2):107-128. https://doi.org/10.1016/j.lithos.2004.04.052

Locock A.J. 2014. An Excel spreadsheet to classify chemical analyses of amphiboles following the IMA 2012 recommendations. *Computers & Geosciences*, **62**:1-11. https://doi.org/10.1016/j.cageo.2013.09.011

Maniar P.D., Piccoli P.M. 1989. Tectonic discrimination of granitoids. *Geological Society of America Bulletin*, **101**(5):635-643. https://doi.org/10.1130/0016-7606(1989)101<0635:TDOG>2.3.CO;2

Marimon R.S., Hawkesworth C.J., Dantas E.L., Trouw R.A., Teixeira W., Hackspacher P.C., Fetter A., Ávila C.A., Volante S., Corrêa Neto A., Bongiolo E.M., Vinagre R., Simon M. 2022. The generation and evolution of the Archean continental crust: The granitoid story in southeastern Brazil. *Geoscience Frontiers*, **13**(4):101402. https://doi.org/10.1016/j.gsf.2022.101402

Martin H. 1986. Effect of steeper Archean geothermal gradient on geochemistry of subduction-zone magma. *Geology*, **14**(9):753-756. https://doi.org/10.1130/0091-7613(1986)14<753:EOSAGG>2.0.CO;2

Martin H. 1987. Petrogenesis of Archaean trondhjemites, tonalites and granodiorites from eastern Finland: major and trace element geochemistry. *Journal of Petrology*, **28**(5):921-953. https://doi.org/10.1093/petrology/28.5.921

Martin H. 1994. The Archean grey gneiss and the genesis of continental crust. Developments in Precambrian Geology, **11**:205-259. https://doi.org/10.1016/S0166-2635(08)70224-X

Martin H. 1999. Adakitic magmas: modern analogues of Archaean granitoids. *Lithos*, **46**(3):411-429. https://doi.org/10.1016/S0024-4937(98)00076-0

Martin H., Moyen J.F., Rapp R. 2009. The sanukitoid series: magmatism at the Archaean-Proterozoic transition. *Earth and Environmental Science Transactions of the Royal Society of Edinburgh*, **100**(1-2):15-33. https://doi.org/10.1017/S1755691009016120

Martin H., Smithies R.H., Rapp R., Moyen J.F., Champion, D. 2005. An overview of adakite, tonalite-trondhjemite-granodiorite (TTG), and sanukitoid: relationships and some implications for crustal evolution. *Lithos*, **79**(1-2):1-24. https://doi.org/10.1016/j.lithos.2004.04.048

Maury R., Sajona F.G., Pubellier M., Bella H., Defant M. 1996. Fusion de la croute oceanique dans les zones de subduction/collision recentes; l'exemple de Mindanao (Philippines). *Bulletin de la Société Géologique de France*, **167**(5):579-595.

Menzies M., Rogers N., Tindle A., Hawkesworth C. 1987. Metasomatic and enrichment processes in lithospheric peridotites, an effect of asthenosphere-lithosphere interaction. In: Menzies M.K., Hawkesworth C.J. (Eds.). *Mantle Metasomatism*. London: Academic Press, p. 313-361.

Miyashiro A. 1978. Nature of Alkalic Volcanic Rock Series. *Contributions to Mineralogy and Petrology*, **66**:91-104. https://doi.org/10.1007/BF00376089

Molina J.F., Castro A., Rodríguez C., Fershtater G. 2015. Calcic amphibole thermobarometry in metamorphic and igneous rocks: New calibrations based on plagioclase/amphibole Al-Si partitioning and amphibole/liquid Mg partitioning. *Lithos*, **232**:286-305. https://doi.org/10.1016/j.lithos.2015.06.027

Moreira I.C., Oliveira E.P., Sousa, D.F.M. 2022. Evolution of the 3.65-2.58 Ga Mairi Gneiss Complex, Brazil: Implications for growth of the continental crust in the São Francisco Craton. *Geoscience Frontiers*, **13**(5):101366. https://doi.org/10.1016/j.gsf.2022.101366

Moyen J.F., Martin H., Jayananda M. 2001. Multi-element geochemical modelling of crust-mantle interactions during late-Archaean crustal growth: the Closepet granite (South India). *Precambrian Research*, **112**(1-2):87-105. https://doi.org/10.1016/S0301-9268(01)00171-1

Moyen J.F., Martin H., Jayananda M., Auvray B. 2003. Late Archaean granites: a typology based on the Dharwar Craton (India). *Precambrian Research*, **127**(1-3):103-123. https://doi.org/10.1016/S0301-9268(03)00183-9

Nachit H., Ibhi A., Abia E., Ben Ohoud M. 2005. Discrimination between primary magmatic biotites, reequilibrated biotites and neoformed biotites. *Comptes Rendus Geosciences*, **337**(16):1415-1420. https://doi.org/10.1016/j.crte.2005.09.002

Navarro M.S., Tonetto E.M., Oliveira E.P. 2017. Peixe Zircon: New Brazilian Reference Material for U-Pb Geochronology by LA-SF-ICP-MS. *Goldschmidt Abstract*. Paris. Available at: https://goldschmidtabstracts.info/abstracts/abstractView?id = 2017005707. Accessed on: Feb. 25, 2023.

Nebel O., Capitanio F.A., Moyen J.F, Weinberg R.F., Clos F., Nebel-Jacobsen Y.J., Cawood P.A. 2018. When crust comes of age: on the chemical evolution of Archaean, felsic continental crust by crustal drip tectonics. *Philosophical Transactions of the Royal Society*, **376**(2132):20180103. https://doi.org/10.1098/rsta.2018.0103

Neves S.P. 2003. Proterozoic history of the Borborema province (NE Brazil): correlations with neighboring cratons and Pan-African belts and implications for the evolution of western Gondwana. *Tectonics*, **22**(4):1031. https://doi.org/10.1029/2001TC001352

Neves S.P. 2011. Atlantica revisited: new data and thoughts on the formation and evolution of a long-lived continent. *International Geology Review*, **53**(11-12):1377-1391. https://doi.org/10.1080/00206814.2010.527676

Neves S.P., Tommasi A., Vauchez A., Carrino T.A. 2021. The Borborema Strike-Slip Shear Zone System (NE Brazil): Large-Scale Intracontinental Strain Localization in a Heterogeneous Plate. *Lithosphere*, **2021**(Spe. 6):6407232. https://doi.org/10.2113/2021/6407232

Nicholls I.A., Ringwood A.E. 1972. Production of silica-saturated tholeiitic magmas in island arcs. *Earth and Planetary Science Letters*, **17**(1):243-246. https://doi.org/10.1016/0012-821X(72)90282-8

Nielsen R. 2022. *Geochemical Earth Reference Model (GERM) partition coefficient (Kd) database*. Available at: https://earthref.org/KDD/. Accessed on: July 23, 2022.

Nockolds S.R., Allen R. 1953. The geochemistry of some igneous rock series. *Geochimica et Cosmochimica Acta*, **4**(3):105-142. https://doi.org/10.1016/0016-7037(53)90055-6

Oliveira E.P., McNaughton N.J., Zincone S.A., Talavera C. 2020. Birthplace of the São Francisco Craton, Brazil: Evidence from 3.60 to 3.64 Ga Gneisses of the Mairi Gneiss Complex. *Terra Nova*, **32**(4):291-289. https://doi.org/10.1111/ter.12460

Oliveira R.G., Medeiros W.E. 2018. Deep crustal framework of the Borborema Province, NE Brazil, derived from gravity and magnetic data. *Precambrian Research*, **315**:45-65. https://doi.org/10.1016/j.precamres.2018.07.004

Pearce J. 1996. Sources and settings of granitic rock. *Episodes*, **19**(4):120-125. https://doi.org/10.18814/epiiugs/1996/v19i4/005

Pearce J.A., Harris N.B.W., Tindle A.G. 1984. Trace Element Discrimination Diagrams for the Tectonic Interpretation of Granitic Rocks. *Journal of Petrology*, **25**(4):956-983. https://doi.org/10.1093/petrology/25.4.956

Petford N., Atherton M. 1996. Na-rich Partial Melts from Newly Underplated Basaltic Crust: the Cordillera Blanca Batholith, Peru. Jou*rnal of Petrology*, **37**(6):1491-1521. https://doi.org/10.1093/petrology/37.6.1491

Pilet S. 2015. Generation of low-silica alkaline lavas: Petrological constraints, models, and thermal implications. In: Foulger G.R., Lustrino M. & King S.D. (Eds.). *The Interdisciplinary Earth:* A Volume in Honor of Don L. Anderson. Geological Society of America Special Paper, **514**; American Geophysical Union Special Publication, **71**:281-304. https://doi.org/10.1130/2015.2514(17)

Prowatke S., Klemme S. 2006. Trace element partitioning between apatite and silicate melts. *Geochimica et Cosmochimica Acta*, **70**(17):4513-4527. https://doi.org/10.1016/j.gca.2006.06.162

Rapp R.P., Shimizu N., Norman M.D., Applegate G.S. 1999. Reaction between slab-derived melts and peridotite in the mantle wedge: experimental constraints at 3.8 GPa. *Chemical Geology*, **160**(4):335-356. https://doi.org/10.1016/S0009-2541(99)00106-0

Rayleigh R.S. 1896. Theoretical considerations respecting the separation of gases by diffusion and similar processes. *Philosophical Magazine*, **42**(259):493-498. https://doi.org/10.1080/14786449608620944

Ribeiro C.V.A. 2019. *Evolução estrutural e metamórfica da porção sul do Domínio São José do Campestre, Província Borborema, NE do Brasil: do Arqueano ao Neoproterozoico*. Undergraduation Monograph, UFRN, Natal, 141 p. Available at: https://repositorio.ufrn.br/handle/123456789/34390. Accessed on: Feb. 25, 2023.

Richter F.M. 1988. A major change in the thermal state of the earth at the Archean e Proterozoic boundary: consequences for the nature and preservation of continental lithosphere. *Journal of Petrology*, **Spe.**(1):39-52. https://doi.org/10.1093/petrology/Special_Volume.1.39

Ridolfi F. 2021. Amp-TB2: an updated model for calcic amphibole thermobarometry. *Minerals*, **11**(3):324. https://doi.org/10.3390/min11030324

Ridolfi F., Renzulli A. 2012. Calcic amphiboles in calc-alkaline and alkaline magmas: thermobarometric and chemometric empirical equations valid up to 1130°C and 2.2 GPa. *Contributions to Mineralogy and Petrology*, **163**:877-895. https://doi.org/10.1007/s00410-011-0704-6

Rieder M., Cavazzini G., D'yakonov Y.S., Frank-Kamenetskii V.A., Gottardi G., Guggenheim S., Koval P.V., Muller G., Neiva A.M.R., Radoslovich E.W., Robert J-L., Sassi F.P., Takeda H., Weiss Z., Wones D.R. 1998. Nomenclature of the micas. *Clays and Clay Minerals*, **46**:586-595. https://doi.org/10.1346/CCMN.1998.0460513

Robinson J.A.C., Wood B.J., Blundy. D. 1998. The beginning of melting of fertile and depleted peridotite at 1.5 GPa. *Earth and Planetary Science Letters*, **155**(1-2):97-111. https://doi.org/10.1016/S0012-821X(97)00162-3

Rubatto D., Hermann, J. 2007. Experimental zircon/melt and zircon/garnet trace element partitioning and implications for the geochronology of crustal rocks. *Chemical Geology*, **241**(1-2):38-61. https://doi.org/10.1016/j.chemgeo.2007.01.027

Rudnick R.L. 1995. Making continental crust. *Nature*, **378**:571-578. https://doi.org/10.1038/378571a0

Sá E.F.J. 1994. *A Faixa Seridó (Provincia Borborema, NE do Brasil) e o seu significado geodinâmico na Cadeia Brasiliana / Pan-Africana.* PhD Thesis, Universidade de Brasília, Brasília, 803 p. Available at: https://mw.eco.br/ig/posg/dout/dout003.htm. Accessed on: Aug. 1st, 2022.

Santosh M., Yang Q.-Y., Teng X., Tang L.I. 2015. Paleoproterozoic crustal growth in the North China Craton: Evidence from the Lüliang Complex. *Precambrian Research*, **263**:197-231. https://doi.org/10.1016/j.precamres.2015.03.015

Sebastian S., Bhutani R., Balakrishnan S., Tomson J.K., Shukla A.D. 2021. Geochemical and isotopic studies of potassic granite from the western Dharwar Craton, southern India: Implications for crustal reworking in the Neoarchean. *Geological Journal*, **56**(6):2930-2949. https://doi.org/10.1002/gj.4085

Sen C., Dunn T. 1994. Dehydration melting of a basaltic composition amphibolite at 1.5 and 2.0 GPa: implications for the origin of adakites. *Contributions to Mineralogy and Petrology*, **117**(4):394-409. https://doi.org/10.1007/BF00307273

Shand S.J. 1943. *Eruptive rocks:* their genesis, composition, classification, and their relation to ore-deposits with a chapter on meteorites. New York: John Wiley & Sons, 444 p.

Smithies R.H. 2000. The Archaean tonalite-trondhjemite-granodiorite (TTG) series is not an analogue of Cenozoic adakite. *Earth and Planetary Science Letters*, **182**(1):115-125. https://doi.org/10.1016/S0012-821X(00)00236-3

Smithies R.H., Champion D.C. 2000. The Archaean High-Mg Diorite Suite: Links to Tonalite-Trondhjemite-Granodiorite Magmatism and Implications for Early Archean Crustal Growth. *Journal of Petrology*, **41**(12):1653-1671. https://doi.org/10.1093/petrology/41.12.1653

Souza Z.S., Dantas E.L. 2008. O Arqueano do Maciço São José de Campestre, Leste do Rio Grande do Norte. *Estudos Geológicos*, **18**(1):122-128.

Souza Z.S., Kalsbeek F., Deng X.D., Frei R., Kokfelt T.F., Dantas E.L., Li J.W., Pimentel M.M., Galindo A.C. 2016. Generation of continental crust in the northern part of the Borborema Province, northeastern Brazil, from Archaean to Neoproterozoic. *Journal of South American Earth Sciences*, **68**:68-96. https://doi.org/10.1016/j.jsames.2015.10.006

Souza Z.S., Martin H., Peucat J.J., Sá E.F.J., Macedo M.H.F. 2007. Calc-alkaline Magmatism at the Archean e Proterozoic Transition: the Caicó Complex Basement (NE Brazil). *Journal of Petrology*, **48**(11):2149-2185. https://doi.org/10.1093/petrology/egm055

Stern C.R., Kilian R. 1996. Role of subducted slab, mantle wedge and continental crust in the generation of adakites from the Andean Austral Volcanic Zone. *Contributions to Mineralogy and Petrology*, **123**(3):263-281. https://doi.org/10.1007/s004100050155

Stern R.A., Hanson G.N. 1991. Archean High-Mg Granodiorite: A derivative of Light Rare Earth Element-Enriched Monzodiorite of Mantle Origin. *Journal of Petrology*, **32**(1):201-238. https://doi.org/10.1093/petrology/32.1.201

Streckeisen A.L. 1976. To each plutonic rock its proper name. *Earth-Science Reviews*, **12**(1):1-33. https://doi.org/10.1016/0012-8252(76)90052-0

Stussi J.M., Cuney M. 1996. Nature of biotites from alkaline, calc-alkaline and peraluminous magmas by Abdel-Fattah M. Abdel-Rahman: a comment. *Journal of Petrology*, **37**(5):1025-1029. https://doi.org/10.1093/petrology/37.5.1025

Sun C., Xu W., Cawood P.A., Tang J., Zhao S, Li Yu, Zhang X. 2019. Crustal growth and reworking: A case study from the Erguna Massif, eastern Central Asian Orogenic Belt. *Scientific Reports*, **9**:17671. https://doi.org/10.1038/s41598-019-54230-x

Sun S.S., McDonough W.F. 1989. Chemical and isotopic systematics of oceanic basalts: implications for mantle composition and processes. In: Saunders A.D., Norry M.J. (Eds.). *Magmatism in the Ocean Basins*. London: Geological Society Special Publications, **42**(1):313-345. https://doi.org/10.1144/GSL.SP.1989.042.01.19

Sylvester P.J. 1994. Archean Granite Plutons. *Developments in Precambrian Geology*, **11**:261-314. https://doi.org/10.1016/S0166-2635(08)70225-1

Taylor S.R., McLennan S.M. 1985. *The continental crust:* its composition and evolution. Oxford: Blackwell, 312 p.

Thomas J.B., Bodnar R.J., Shimizu N., Sinha A.K. 2002. Determination of zircon/melt trace element partition coefficients from SIMS analysis of melt inclusions in zircon. *Geochimica et Cosmochimica Acta*, **66**(16):2887-2901. https://doi.org/10.1016/S0016-7037(02)00881-5

Thorpe R.S., Francis P.W., O'Gallaghan L. 1984. Relative roles of source composition, fractional crystallization and crustal contamination in the petrogenesis of Andean volcanic rock. *Philosophical Transactions of the Royal Society*, **310**(1514):675-692. https://doi.org/10.1098/rsta.1984.0014

Van Schmus W.R., Brito Neves B.B., Williams I.S., Hackspacher P.C., Fetter A.H., Dantas E.L., Babinski M. 2003. The Seridó group of NE Brazil, a late Neoproterozoic pre- to syn-collisional basin in West Gondwana: insights from SHRIMP U-Pb detrital zircon ages and Sm-Nd crustal residence (T_{DM}) ages. *Precambrian Research*, **127**(4):287-327. https://doi.org/10.1016/S0301-9268(03)00197-9

Van Schmus W.R., Kozuch M., Brito Neves B.B. 2011. Precambrian history of the Zona Transversal of the Borborema Province, NE Brazil: insights from Sm-Nd and U-Pb geochronology. *Journal of South American Earth Sciences*, **31**(2-3):227-252. https://doi.org/10.1016/j.jsames.2011.02.010

Van Schmus W.R., Oliveira E.P., Silva Filho A.F., Toteu S.F., Penaye J., Guimarães I.P. 2008. Proterozoic links between the Borborema Province, NE Brazil, and the Central African Fold Belt. *Geological Society, London, Special Publications*, **294**(1):69-99. https://doi.org/10.1144/SP294.5

Vanderhaeghe O., Guergouz C., Fabre C., Duchêne S., Baratoux D. 2019. Secular cooling and crystallization of partially molten Archaean continental crust over 1 Ga. *Comptes Rendus Geoscience*, **351**(8):562-573. https://doi.org/10.1016/j.crte.2019.07.002

Vauchez A., Neves S., Caby R., Corsini M., Egydio-Silva M., Arthaud M., Amaro V.E. 1995. The Borborema shear zone system, NE Brazil. *Journal of South America Earth Sciences*, **8**(3-4):247-266. https://doi.org/10.1016/0895-9811(95)00012-5

Viegas M.C.D. 2007. *Síntese geológica do Leste do Rio Grande do Norte na escala 1: 250.000*. Undergraduation Monograph, UFRN, Natal, 78 p.

Viegas M.C.D., Souza Z.S. 2007. Síntese Geológica do leste do Rio Grande do Norte na escala 1:250.000. In: XI Simpósio Nacional de Estudos Tectônicos and V International Symposium on Tectonics of the SBG, Natal. *Proceedings…* p. 218-220.

Wasylenki L.E., Baker M.B., Kent A.J.R., Stolper E.M. 2003. Near-solidus melting of the shallow upper mantle: partial melting experiments on depleted peridotite. *Journal of Petrology*, **44**(7):1163-1191. https://doi.org/10.1093/petrology/44.7.1163

Watson E.B., Harrison T.M. 1983. Zircon saturation revisited: temperature and composition effects in a variety of crustal magma types. *Earth and Planetary Science Letters*, **64**(2):295-304. https://doi.org/10.1016/0012-821X(83)90211-X

Wedepohl K.H. 1995. The composition of the continental crust. *Geochimica et Cosmochimica Acta*, **59**(7):1217-1232. https://doi.org/10.1016/0016-7037(95)00038-2

Whitney D.L., Evans B.W. 2010. Abbreviations for names of rock-forming minerals. *American Mineralogist*, **95**(1):185-187. https://doi.org/10.2138/am.2010.3371

Wiedenbeck M.A.P.C., Alle P., Corfu F., Griffin W.L., Maier M., Oberli F.V., Roddinick J.C., Spiegel W. 1995. Three natural zircon standards for U-Th-Pb, Lu- Hf, trace element and REE analyses. *Geostandards and Geoanalytical Research*, **19**(1):1-23. https://doi.org/10.1111/j.1751-908X.1995.tb00147.x

Wilson M. 1989. *Igneous petrogenesis:* global tectonic approach. London: Chapman & Hall, 466 p.

Yang X.M. 2017. Estimation of crystallization pressure of granite intrusions. *Lithos*, **286-287**:324-329. https://doi.org/10.1016/j.lithos.2017.06.018

Yang X.M., Drayson D., Polat A. 2019. S-type granites in the western Superior Province: a marker of Archean collision zones. *Canadian Journal of Earth Sciences*, **56**(12):1409-1436. https://doi.org/10.1139/cjes-2018-0056

Yang X.M., Lentz D.R., Chi G. 2021. Ferric-ferrous iron oxide ratios: Effect on crystallization pressure of granites estimated by Qtz-geobarometry. *Lithos*, **380-381**:105920. https://doi.org/10.1016/j.lithos.2020.105920